Tau, amyloid-β and α-synuclein co-pathologies synergistically enhance neuroinflammation and neuropathology

Jhodi M. Webster[1, 2], Ya-Ting Yang[1, 2], Aidan T. Miller[1], Asta Zane[1], Kasandra Scholz[1], William J. Stone[1], Nikhita Mudium[1], Nicole J. Corbin-Stein[1,2], Woong-Jai Won[1], Anna C. Stoll[1], Kelsey M. Greathouse[1], Noelle H. Cooper[1], Lillian F. Long[1], Phaedra N. Manuel[1], Jeremy H. Herskowitz[1], Talene A. Yacoubian[1], Daniel J. Tyrrell[3], Ivette M. Sandoval[5], Fredric P. Manfredsson[2, 5], Jeffrey H. Kordower[2,6], and Ashley S. Harms[1, 2]*

Author affiliations:

[1]University of Alabama at Birmingham, Department of Neurology, Killion Center for Neurodegeneration and Experimental Therapeutics, Birmingham, AL, 35294

[2]Aligning Science Across Parkinson's (ASAP) Collaborative Research Network, Chevy Chase, MD, 20815

[3]University of Alabama at Birmingham, Department of Pathology, Division of Molecular and Cellular Pathology, Birmingham, AL, 35294

[4]Neurodegenerative Diseases Research Unit, Biogen, Cambridge, MA, 02142

[5]Barrow Neurological Institute, Department of Translational Neuroscience; Phoenix, AZ, 85013

[6]Arizona State University, ASU-Banner Neurodegenerative Disease Research Center, Bio-design Institute, Tempe, AZ, 85281

***Correspondence to:**

Ashley S. Harms

University of Alabama at Birmingham, 1719 6th Ave South, Birmingham, Alabama 35294

anharms@uab.edu

Running title: Co-pathologies drive neuroinflammation in disease

Keywords: co-pathologies, neuroinflammation, α-synuclein, tau, amyloid beta, T cells, microglia

Summary

Webster et al. demonstrate that co-occurring Alzheimer's and Parkinson disease protein pathologies, common in cognitively impaired patient populations, amplify proteinopathy and synergistically enhance CNS neuroinflammatory responses and neurodegeneration. This work supports the need for combinatorial therapeutic strategies and positions neuroinflammation as an important link for co-pathology enhanced neurodegeneration.

Abstract

Alzheimer's (AD) and Parkinson disease (PD) pathology often co-occur. Amyloid-β and phosphorylated tau are found in 30-50% of idiopathic PD cases, while α-synuclein inclusions are present in 50% of AD cases. These co-pathologies are linked to increased mortality and earlier onset of cognitive decline. Immune activation is a hallmark of these neurodegenerative diseases, but current models primarily examine each pathology in isolation. How these co-pathologies drive inflammation and neuronal loss remains poorly understood. We therefore developed a mouse model combining tau, amyloid-β, and α-synuclein. We found that co-pathologies synergistically trigger an amplified neuroimmune response, with expanded populations of $CD4^+$ and $CD8^+$ tissue-resident memory T cells and $CD68^+$ microglia, compared to single pathologies. These changes were abundant in the hippocampus and cortex, regions with elevated protein pathology load and enhanced neuronal loss. Our findings demonstrate that co-pathologies enhance proteinopathy and synergistically enhance immune activation and neurodegeneration, suggesting that combinatorial therapeutic strategies that target both co-pathologies and inflammation, may be disease modifying.

Introduction

In addition to the progressive loss of neurons and brain atrophy, neurodegenerative diseases share the common feature of pathogenic protein accumulation and worsening cognitive decline. These proteins include α-synuclein (α-syn) inclusions found in Lewy bodies and Lewy neurites in Parkinson disease (PD) and Parkinson disease dementia (PDD), extracellular amyloid-β (Aβ) plaques and phosphorylated-tau (tau) inclusions in the form of intracellular neurofibrillary tangles in Alzheimer's disease (AD) (Goedert, 1993, Joachim and Selkoe, 1989, Spillantini et al., 1997). Although these proteins are pathologically associated with their respective diseases, there is evidence for the overlap of pathology and symptoms. The presence of these AD-related pathologies, found in 50-80% of PD brains (Irwin et al., 2017, Irwin et al., 2018, Jellinger, 2002, Jellinger, 2003, Jellinger, 2020, Kotzbauer et al., 2012, Robinson et al., 2018, Spires-Jones et al., 2017), has been a significant contributor to exacerbated disease progression and dementia onset in patients with PD (Compta et al., 2014, Kotzbauer et al., 2012). Similarly, Lewy bodies have been found in the brains of AD patients (Twohig and Nielsen, 2019, van der Gaag et al., 2024) and this a-syn co-pathology has been shown to promote amyloid-driven tau accumulation in AD brains (Franzmeier et al., 2025). The co-expression of these pathologies has been linked to earlier onset of cognitive decline and higher rate of mortality (Coughlin et al., 2019, Kraybill et al., 2005, Mak et al., 2024, Malek-Ahmadi et al., 2019). This exacerbated disease phenotype under co-pathology conditions suggests potential synergy between α-syn, tau and Aβ, however the disease-progressing mechanisms of this co-expression remain unknown.

Previously, multi-pathology mouse models have also implicated potential interactions between pathologies. In dementia with Lewy body (DLB)-AD and PD-AD mouse models, combined tau, Aβ and α-syn pathologies enhanced aggregation and spreading of pathology beyond

70 single pathology effects (Bassil et al., 2020, Bassil et al., 2021, Clinton et al., 2010).
71 Neurodegeneration, however, was only shown to be influenced by Aβ and α-syn co-pathology in
72 5XFAD mice injected with α-syn mouse pre-formed fibrils (PFFs) (Bassil et al., 2020).
73 Additionally, neuroinflammation in the presence of the co-pathologies was not fully assessed in
74 these animal models. As such, it remains unknown how these co-pathologies may promote the
75 immune cell activation leading to the neurodegeneration and sustained aggregated protein
76 pathology seen in human disease.

77 Neuroinflammation, driven by microglia and CNS-resident macrophages, infiltrating
78 lymphocytes, and monocytes, is a key contributor to neuronal loss and neurodegenerative disease
79 progression. $CD4^+$ and $CD8^+$ T cells are found in the brains (Itagaki et al., 1988, Merlini et al.,
80 2018, Rogers et al., 1988, Togo et al., 2002) and cerebrospinal fluid (Gate et al., 2020) of AD, PD
81 and DLB patients (Brochard et al., 2009, Sulzer et al., 2017, Yan et al., 2021), along with
82 activation of myeloid cells, including microglia, macrophages and monocytes. In AD, Aβ plaques
83 trigger and can interact with microglia to adopt a phagocytic but dysfunctional disease-associated
84 microglia (DAM) phenotype (Ries and Sastre, 2016, Zhao et al., 2018) while Aβ-specific T cells
85 infiltrate the brain and exacerbate tau pathology and neurodegeneration (Keren-Shaul et al., 2017).
86 Tau pathology also triggers a pro-inflammatory phenotype in microglia through receptor binding
87 (Pampuscenko et al., 2023) and promotes CNS-specific changes in T cell reactivity (Chen et al.,
88 2023). In PD, α-syn also interacts with toll-like receptors (TLRs) on microglia to promote release
89 of inflammatory cytokines (Karpenko et al., 2018), while T cells target α-syn epitopes in the
90 substantia nigra pars compacta (SNpc) (Ma et al., 2025, Sulzer et al., 2017). While these cells aid
91 in immune surveillance during homeostatic conditions, in chronic disease, microglia and T cells
92 may adopt pro-inflammatory phenotypes and contribute to neurotoxicity and exacerbated neuronal

damage (Altendorfer et al., 2022, Galiano-Landeira et al., 2020, Hefendehl et al., 2014, Kimura et al., 2024, Wang et al., 2021). Although recent work has highlighted enhanced microglial activation in mixed DLB + AD patients (van Wetering et al., 2024), how combined tau, Aβ and α-syn pathologies may synergistically influence the full neuroinflammatory response remains unclear.

To further understand how co-pathologies drive neurodegeneration, we aimed to determine whether the combined presence of tau, Aβ and α-syn promotes neuroinflammation, protein aggregation and neuronal loss through synergistic effects. To do this, we developed a co-pathology mouse model, generated by injection of adeno-associated virus (AAV)-double mutant tau into the entorhinal cortex and α-syn mouse PFFs into the striatum of J20 amyloid over-expressing transgenic mice (Mucke et al., 2000). This model allowed us to evaluate the impact of multiple pathological proteins on innate and adaptive immune responses as well as neurodegeneration within vulnerable regions, including the hippocampus. We found that the presence of co-pathologies not only promotes protein pathology deposition compared to single pathology models, but also triggered synergistic neuroinflammatory responses and subsequent enhanced neuronal loss in the hippocampus. These findings support post-mortem co-pathology data (van Wetering et al., 2024) and model tau, Aβ and α-syn synergizing to enhance key immunopathogenic processes that may contribute to neurodegenerative disease progression.

Results

Co-pathologies enhance Aβ plaques and α-syn inclusions

The co-expression of tau, Aβ and α-syn has been reported in the limbic and cortical regions, particularly in the hippocampus and neocortex in human postmortem studies from DLB, AD and PDD brains (Colom-Cadena et al., 2013, Ferman et al., 2018, Kouli et al., 2020). To model this *in*

116 *vivo* in mice, we generated a co-pathology model incorporating tau, Aβ and α-syn and compared
117 data obtained in this co-pathology model with mice only expressing a single pathology. As a Tau
118 single pathology control, tau pathology was induced in non-transgenic (NTG), C57BL/6J mice via
119 bilateral entorhinal cortex injection of an AAV expressing human tau with two mutations (AAV9-
120 Tau) (Figure 1a). To model Aβ single pathology, J20 transgenic (Tg) mice (Mucke et al., 2000),
121 which overexpress human mutant amyloid precursor protein (APP^{mut}) and develop Aβ plaques in
122 the hippocampus and cortex (Figure 1b), were aged to 6 months old. Lastly, for α-syn single
123 pathology control, 12–14-week-old NTG mice received bilateral injections of mouse α-syn PFFs
124 into the dorsal lateral striatum (Figure 1c). To create a model of co-pathology, age-matched J20
125 mice were bilaterally injected with both α-syn PFFs into the basal lateral striatum and AAV9-Tau
126 into the entorhinal cortex during one stereotaxic surgery session, combining tau, Aβ and α-syn
127 pathologies in one model (Figure 1d) resulting in co-pathologies in the hippocampus and cortex.
128
129 Co-pathologies exhibit synergistic interactions that promote the aggregation and accumulation of
130 disease-associated protein (Franzmeier et al., 2025, Irwin et al., 2013, Robinson et al., 2018,
131 Sengupta and Kayed, 2022). To determine whether the presence of co-pathology enhances α-syn,
132 tau and Aβ individually, single pathology controls and co-pathology brains were assessed for
133 histological and biochemical markers of protein pathology at 3- and 6-months post-induction
134 (MPI) using immunohistochemistry (IHC), western blotting, and enzyme linked immunosorbent
135 assay (ELISA) (Figure 2a). AT-8^{+} neurons were immunolabeled in the cortex and hippocampus of
136 6-month-old (3MPI) (Figure 2b) and 9-month-old (6MPI) (Supplemental Figure 1a) Tau single
137 pathology and co-pathology mice. Total tau protein expression at 3MPI and 6MPI in Triton X-100
138 soluble and insoluble fractions of the hippocampus and cortex was assessed using western blot

139 (Figure 2c). No significant difference in tau pathology was observed between Tau single pathology
140 and co-pathology groups at 3MPI, but a significant difference in tau accumulation was observed
141 at 6MPI. At 6MPI, the presence of co-pathologies enhanced soluble tau in the hippocampus of co-
142 pathology mice compared to single pathology controls (Figure 2d). Collectively, these data
143 suggest that tau pathology accumulates in the hippocampus and cortex over time, and highlight
144 the presence of co-pathology enhanced soluble tau in the hippocampus of mice at 6MPI.
145
146 Using an antibody specific to Aβ aggregation, $A\beta^{+}$ plaques were observed via
147 immunohistochemistry in the hippocampus and cortex of co-pathology and J20 (Aβ) single
148 pathology controls at 3MPI (Figure 2e) and 6MPI (Supplemental Figure 1b). As assessed by
149 ELISA, insoluble $A\beta_{1\text{-}42}$ protein decreased between 3MPI and 6MPI. At 3MPI, insoluble $A\beta_{1\text{-}42}$
150 levels were significantly increased in the hippocampus and cortex of co-pathology brains
151 compared to J20 single pathology controls indicating the presence of co-pathologies enhanced
152 early insoluble $A\beta_{1\text{-}42}$ (Figure 2f).
153
154 $pSer129^{+}$ α-syn inclusions were visible within the neurites and cell bodies in the hippocampus and
155 cortex of PFF (α-syn) single pathology and co-pathology mice at 3MPI (Figure 2g) and 6MPI
156 (Supplemental Figure 1c). Total α-syn protein expression at 3MPI and 6MPI in the hippocampus
157 and cortex was assessed via western blot (Figure 2h). Similar to $A\beta_{1\text{-}42}$, total α-syn protein was
158 decreased in the hippocampus and cortex at 6MPI, compared to 3MPI. At 3MPI, there was an
159 increase in soluble α-syn in the cortex of co-pathology brains compared to PFF single pathology
160 (Figure 2i) controls.
161

162 All together, these results highlight that tau, Aβ and α-syn as co-pathologies may enhance
163 accumulation of one another indicating that the location and timing of pathology deposition may
164 be an important factor.
165

166 **Neuronal loss is driven by the co-expression of tau, Aβ and α-syn pathologies**

167 Neurodegeneration, including changes in synaptic density and the subsequent death of neurons,
168 occurs prior to severe onset of symptoms associated with neurodegenerative diseases. Such
169 symptoms include cognitive and motor impairments (Braak et al., 2003, DeKosky and Scheff,
170 1990, Greffard et al., 2006, Selkoe, 2002). Given the involvement of tau, Aβ and α-syn in
171 neurodegenerative diseases and their strongly association with these symptoms, we performed
172 open field, Barnes maze, rotarod and pole behavioral tests to assess for cognitive and motor deficits
173 in the model at 6MPI (Supplemental Figure 2). Sham mice, NTG animals bilaterally injected with
174 α-syn monomer and AAV9-GFP into the striatum and entorhinal cortex, respectively, were used
175 as a surgical control for co-pathology mice. Behavioral changes were observed with co-pathology
176 mice making significantly more errors and reduced time to commit errors compared to sham mice
177 in the Barnes maze test, but no significant difference was observed when compared to single
178 pathology controls despite a faster time to the goal quadrant compared to J20 mice (Supplemental
179 Figure 2a). Co-pathology mice showed increased turnaround and total time on the pole test
180 compared to sham mice (Supplemental Figure 2b). The open field test also showed increased
181 distance traveled by the co-pathology mice compared to sham (Supplemental Figure 2c). However,
182 overall co-pathology mice showed no differences in movement as shown by the rotarod test
183 (Supplemental Figure 2d). In summary, co-pathologies did not produce any major effects on motor
184 or cognitive function in mice. This may be due to the intrinsic neural hyperexcitability of the J20

185 mouse model, which is known to drive a hyperactive behavioral phenotype (Busche et al., 2012,
186 Shabir et al., 2020).

187 Dendritic spines are important for learning and memory and their morphology is an indicator of
188 synaptic integrity and plasticity, both of which are disrupted in neurodegenerative diseases
189 associated with cognitive decline (Bourne and Harris, 2008, Knobloch and Mansuy, 2008, Spires-
190 Jones and Hyman, 2014). To test the hypothesis that tau, Aβ and α-syn co-pathologies synergize
191 to exacerbate synaptic damage, we performed a detailed morphometric analysis of dendritic spines
192 on Lucifer yellow labelled CA1 pyramidal neurons in the hippocampus across single and co-
193 pathology brains. Our analysis showed that co-pathologies are associated with distinct changes to
194 spine structure in the hippocampus. Specifically, co-pathology spines were significantly shorter in
195 length compared to α-syn single pathology (Supplemental Figure 3a,b). Interestingly, spine
196 volume on basal dendrites was increased in the hippocampus of co-pathology mice relative to
197 brains with only Aβ or α-syn pathology, which may indicate a compensatory but dysfunctional
198 state (Supplemental Figure 3c). Collectively, these findings suggest the presence of co-pathologies
199 alters synapse integrity, which may be important for driving neuronal loss and cognitive decline.

200 Neuronal loss is a hallmark feature observed in both AD and PD, with region-specific vulnerability
201 depending on disease pathology (Double, 2012, Giguère et al., 2018, Mrdjen et al., 2019, Olajide
202 et al., 2021). Previous work, however, has only assessed neuronal loss in the context of α-syn and
203 Aβ as co-pathologies (Bassil et al., 2021). Given this and our synaptic morphology findings, we
204 next hypothesized that co-expression of tau, Aβ and α-syn may enhance neuronal loss in the
205 hippocampus. To assess neurodegeneration, we performed unbiased stereology on neurons in the
206 hippocampus of co-pathology and single pathology controls at 6MPI (Figure 3a). Immunostaining
207 for NeuN+ neurons in the hippocampus of single pathology and co-pathology mice showed a

208 distinct loss of neurons in the CA1 region of co-pathology brains (Figure 3b). Although there was
209 an expected loss of neurons in the CA1 or CA3 regions of the hippocampus of each of the single
210 pathology brains compared to their controls (Supplemental Figure 4a,b), we found enhanced loss
211 (20-30%, $p<0.001$) of $NeuN^+$ neurons in the CA1 region of the hippocampus in the co-pathology
212 mice compared to tau, Aβ or α-syn single pathology mice (Figure 3c). Within the CA3, co-
213 pathology mice showed significant loss (20-25%, $p<0.01$) compared to single tau and α-syn
214 controls only (Figure 3d). Along with cognitive decline, patients with neurodegenerative disease
215 also exhibit significant motor deficits, mostly due to the loss of neurons in motor-related cortical
216 regions or loss of dopaminergic neurons in the SNpc (Braak et al., 2003, Buchman and Bennett,
217 2011). In the SNpc at 6MPI, the loss of tyrosine hydroxylase (TH)-positive neurons was
218 significantly enhanced in the co-pathology model compared to that in the Aβ single pathology
219 animals. However, in comparison to tau and α-syn mice, the co-pathologies did not enhance TH+
220 cell loss (Supplemental Figure 4c,d). Taken together, these results highlight a synergistic
221 interaction between tau, Aβ and α-syn co-pathologies that exacerbates neurodegeneration in the
222 hippocampus.

223

224 **Co-pathologies enhance microglial activation and infiltration of peripheral monocytes**

225 Given that tau, Aβ and α-syn pathologies are individually associated with microglia activation and
226 infiltration of peripheral myeloid cells in *in vivo* models (Harms et al., 2018, Heneka et al., 2013,
227 Maphis et al., 2015) and in human disease(van Wetering et al., 2024), we aimed to determine the
228 role of co-pathologies in enhancing innate immune responses in the CNS. Co-pathology and single
229 pathology models were induced as previously stated using 12–14-week-old J20 Tg or NTG
230 littermates (Figure 1). At 3MPI, hippocampal and cortical regions were dissected from co-

231 pathology and single pathology controls for IHC analysis, mononuclear cell isolation and flow
232 cytometry (Figure 4a). Using fluorescent IHC we immunolabeled Iba1, a marker used to visualize
233 morphology of both homeostatic and activated microglia, in single pathology and co-pathology
234 brains. Compared to tau, Aβ and α-syn single pathology brains, an increased number of "activated"
235 Iba1^{+} cells were observed in the hippocampus of co-pathology mice (Figure 4b). Using flow
236 cytometry, CD11b^{+}CD45^{+} double positive myeloid cells were gated to analyze CNS resident
237 microglia (CD45^{mid}CX3CR1^{+}) and CD45^{hi} CNS macrophage populations (including infiltrating
238 monocytes and other CNS resident macrophages) (Supplemental Figure 5a; Figure 4c). In the
239 hippocampus and cortex, the number of microglia and CD45^{hi} macrophages increased with co-
240 pathologies (Figure 4d,e) compared to single pathology controls. Within this CD45^{hi} population,
241 Ly6C^{hi} infiltrating monocytes and CNS resident macrophages were also increased in the
242 hippocampus of co-pathology brains compared to tau, Aβ and α-syn single pathology brains
243 (Supplemental Figure 5d,e).
244
245 Given that microglia exhibit heterogeneity in health and disease based on their activation state, we
246 next profiled markers of proliferation and activation to define the specific phenotypes associated
247 with co-pathologies in the hippocampus and cortex. For this, we used CD68, a marker of
248 phagocytic activity and MHCII, a key mediator of antigen presentation to distinguish activated,
249 antigen presenting and/or phagocytic microglia. In co-pathology brains, the overall number of
250 MHCII^{+} and MHCII^{+}CD68^{+} microglia decreased compared to single pathologies (Supplemental
251 Figure 5f,g). Conversely, MHCII^{-}CD68^{+} microglia were significantly increased in the
252 hippocampus and cortex of co-pathology mice compared to single pathology brains (Supplemental
253 Figure 5f,g), indicating a shift towards a phagocytic response. To confirm whether these

254 phagocytic microglia are driving the pro-inflammatory response due to co-pathologies, we
255 assessed proliferation (Ki67 expression) and pro-inflammatory phenotype (TLR2 expression) on
256 MHCII^{+}CD68^{+} (inflammatory phagocytes) and MHCII-CD68+ (pure phagocytes) populations for
257 functional analysis (Figure 4f). MHCII^{+}CD68^{+} microglia showed decreased expression of Ki67
258 and TLR2 (Figure 4g,h), which could imply reduced antigen presentation in co-pathology brains.
259 On the other hand, MHCII^{-}CD68^{+} microglia showed robust proliferation and TLR2^{+} expression in
260 the hippocampus and cortex of co-pathology brains compared to single pathology controls (Figure
261 4i,j). Overall, these results indicate that at 3MPI, tau, Aβ and α-syn co-pathologies synergistically
262 promote morphological and proliferative changes in microglia, translating to a more activated,
263 phagocytic state, likely to prioritize clearance of the increased protein pathology load seen in co-
264 pathology brains.
265

266 **Co-pathologies promote T cell invasion and resident memory phenotype**

267 Given the enhanced myeloid cell responses with co-pathologies (van Wetering et al., 2024) and
268 the contribution of peripheral CD4^{+} and CD8^{+} T cells to neurodegeneration *in vivo* (Brochard et
269 al., 2009, Ferretti et al., 2016) and in human disease (Gate et al., 2021, Haage and De Jager, 2022,
270 Yamakawa and Rexach, 2024), we aimed to determine if T cell responses were synergistically
271 enhanced by co-pathologies. Following co-pathology induction, brains were sectioned for IHC or
272 dissected for single-cell isolation at 3MPI (Figure 5a). Using IHC, we show the presence of co-
273 pathologies enhanced infiltration of CD3^{+} (Supplemental Figure 6a) or CD4+ (Figure 5b) T cells
274 into the hippocampus compared to tau, Aβ and α-syn single pathology brains. Utilizing
275 mononuclear cell isolation and spectral flow cytometry, our results revealed that there were
276 significantly more CD4^{+} and CD8^{+} T cells in the hippocampus and cortex of co-pathology brains

compared tau, Aβ and α-syn single pathology mice (Figure 5c-e). This data demonstrates that the presence of co-pathologies enhances the presence of both helper ($CD4^+$) and cytotoxic ($CD8^+$) T cells into the brain. These data suggest that adaptive immune mechanisms observed prior to neurodegeneration may be important or significantly contribute to enhanced hippocampal neurodegeneration observed with co-pathology.

Tissue resident memory (Trm) T cells have been observed in human post mortem tissue in neurodegenerative diseases such as AD and PD (Gate et al., 2020, Su et al., 2023) where they accumulate in the brain and contribute to chronic inflammation and neuronal loss (Kimura et al., 2024, Yamakawa and Rexach, 2024). Using cell surface markers expressed by Trm T cells ($CD69^+$ and $CD103^+$) and $CD44^+$ (effector, activated T cells that are antigen experienced), we examined both $CD4^+$ and $CD8^+$ Trm in the hippocampus and cortex of co-pathology mice compared to single pathology mice at 3MPI. In both brain regions, co-pathologies promoted a significant expansion of both $CD4^+$ and $CD8^+$ Trm ($CD62L^-CD44^+CD69^+CD103^+$) relative to all single pathologies (Supplemental Figure 6b,c). $CD44^+CD4^+$ T cells and $CD4^+CD69^+$ Trm (Figure 5f-h) increased by 10+ fold in co-pathology brains relative to single pathology controls. $CD44^+CD8^+$ T cells and $CD8^+CD69^+CD103^+$ Trm were increased over 100-fold in co-pathology brains compared to single pathologies (Figure 5i-k). Our findings illustrate a synergistic expansion of Trm T cells, in CD4 T cells but more robust in CD8 T cells, indicating that tau, Aβ and α-syn co-pathologies promote the long-term expansion and survival of antigen-experienced T cells within the brain prior to overt neurodegeneration.

Discussion

300 Tau, Aβ and α-syn are pathological hallmarks of neurodegenerative diseases associated
301 with cognitive decline, however, how these protein pathologies synergize to enhance
302 neurodegeneration remains unknown. Using a novel mouse model of co-pathology incorporating
303 tau, Aβ and α-syn co-pathologies, our results demonstrate synergistic activation of innate and
304 adaptive immune responses in areas with co-expression of these accumulated proteins. At 3MPI,
305 Aβ pathology and soluble alpha-synuclein levels were increased compared to the single pathology
306 controls along with a robust neuroinflammatory response, including increased microglial cell
307 number and changes in activation state, infiltration of T cells and enhanced Trm signature in the
308 hippocampus and cortex. The synergistic, not merely additive, effect of co-pathologies creates a
309 pro-inflammatory CNS environment that, in turn, enhances disease pathogenesis. Building on our
310 previous work demonstrating that blocking neuroinflammation can prevent neuronal loss in
311 models of neurodegeneration (Corbin-Stein et al., 2024, Williams et al., 2018), we propose that
312 this is largely mediated through exacerbated innate and adaptive immune responses, positioning
313 neuroinflammation as an important link between protein aggregation and neuronal loss, and a
314 prime target for combination therapy.

315 Previous studies have established that multiple protein pathologies in mouse models can
316 interact to exacerbate disease phenotypes. DLB-AD mice (3xTg AD mice crossed with α-syn
317 A53T mice) yielded the first triple pathogenic model with worsened cognitive decline, however,
318 there were no observed changes in microglial reactivity (Clinton et al., 2010). Combining AD-
319 derived tau with α-syn PFFs further enhanced tau pathology and its spread relative to controls
320 (Bassil et al., 2020). Similarly, to dissect the interaction between α-syn and Aβ, 5xFAD mice were
321 stereotaxically injected with mouse α-syn PFFs to develop a 'PD-AD' mouse, that exhibited
322 enhanced hippocampal neuronal loss, as the only mutli-pathology mouse model to assess

323 neurodegeneration (Bassil et al., 2021). Lastly, crossing APP/PS1 mice with mutant P301L tau
324 mice has shown increased formation of Aβ plaques and tau tangles (Lewis et al., 2001). The
325 mechanism underlying this has been linked to Aβ plaques activating kinases, which leads to
326 mislocalization of tau, and subsequent hyperphosphorylation (Lewis et al., 2001, Shipton et al.,
327 2011). Results from these studies demonstrate that the presence of additional pathologies promote
328 each other's aggregation and accelerate cognitive decline in mice and as such, complements the
329 work done in human postmortem studies showing co-pathology expression correlated to aging,
330 neuroinflammation and neurodegeneration (Schneider et al., 2007, van Wetering et al., 2024).
331 However, likely due to the design of these models, a critical question remains unanswered: whether
332 and how tau, Aβ and α-syn synergize together as co-pathologies to trigger amplified immune
333 responses that directly influences enhanced neurodegeneration.

334 Within, we created a novel co-pathology mouse model to answer this question and
335 determine the effect of co-pathologies on pathological protein deposition, neuroinflammation, and
336 neurodegeneration. To model this pathological overlap seen in neurodegenerative disease, we
337 combined the AAV9-double mutant Tau (tau) and α-syn mouse PFFs (α-syn) in the same J20
338 APP^{mut} mouse (Aβ). The J20 model provides moderate, localized Aβ pathology beginning at
339 approximately 4 months old (Mucke et al., 2000), while AAV-driven tau propagates from the
340 entorhinal cortex to the hippocampus and cortex to model tau spread. As endogenous mouse tau
341 does not aggregate or form neurofibrillary tangle-like inclusions (Andorfer et al., 2003, Duff et al.,
342 1996, Lewis et al., 2000), it was important to induce the pathology in a region like the entorhinal
343 cortex, where localization allows for the propagation and subsequent expression of intracellular
344 phosphorylated tau within the hippocampus and neighboring cortices. α-syn mouse PFFs induce
345 Lewy-like inclusions with intracellular aggregation and spreading throughout the limbic and

346 cortical regions. While AAVs that overexpress α-syn in transduced regions have been used to
347 model PD (Decressac et al., 2012, Elabi et al., 2021, Karikari et al., 2022, Schonhoff et al., 2023),
348 these overexpression vectors typically lack the disease-like spreading pathology and only
349 recapitulate the molecular pathology of SNCA gene duplication/triplication carriers (Gómez-
350 Benito et al., 2020, Pinto-Costa et al., 2023). While this model does not fully recapitulate the spatial
351 distribution and temporal onset of pathology seen in human disease, it was designed to induce tau,
352 Aβ and α-syn pathology within their classically affected brain regions. Like most protein
353 overexpression and seeding models, it carries limitations, including the non-physiological levels
354 and a lack of gradual disease progression. While postmortem tissues offer a snapshot in time of
355 disease-driving pathology, modeling *in vivo* is needed to study interactions. Despite these caveats,
356 this model of co-pathology offers a useful tool to investigate how these pathologies synergize to
357 drive neurodegeneration and neuropathology.

358 Within, we show that the presence of co-pathologies significantly increases protein load in
359 the brain. At 3MPI, the co-expression of tau, Aβ and α-syn in the hippocampus and cortex led to
360 a significant increase in insoluble $A\beta_{1-42}$ load compared to J20 single pathology brains, as well as
361 soluble α-syn in the compared to PFF single pathology brains. These findings are consistent with
362 previously reports showing enhanced Aβ and α-syn protein pathology load under co-pathology
363 conditions (Bassil et al., 2020, Bassil et al., 2021). At this early timepoint, tau levels remained low
364 and unchanged across groups in both the hippocampus and cortex, likely reflecting the slower
365 kinetics of tau seeding and propagation mechanisms (de Calignon et al., 2012) from the entorhinal
366 cortex to interconnected brain regions. In line with this known phenomenon, by 6MPI we observed
367 that soluble tau was significantly increased in the hippocampus and cortex of co-pathology mice
368 relative to Tau single pathology controls while insoluble tau levels remained comparable between

369 groups at this later timepoint. This suggests that the early presence of Aβ pathology (already
370 existing at time induction) together with rapidly seeded α-syn pathology creates an environment
371 that promotes the formation of soluble tau species, including hyperphosphorylated monomers and
372 pathogenic oligomers. Previous work has also shown that at later stages, tau burden remains
373 similar and unchanged in a 5XFAD + αsyn multi-pathology model compared to control mice. Our
374 co-pathology mouse model differs in that tau pathology is driven by interaction of mutant tau
375 fragments with endogenous tau to seed rather than endogenous overexpression in the 5XFAD
376 model, producing slower spread of pathology that manifests at the later timepoint of 6 months
377 post-induction. In contrast to tau, we observed a decrease in overall $A\beta_{1-42}$ and α-syn load at 6MPI,
378 which is likely attributable to substantial loss of neurons in the hippocampus that would have
379 produced this pathology at this stage. Collectively, these findings illustrate that co-pathologies
380 enhance proteinopathy in the hippocampus and cortex and future combinatorial approaches may
381 be an effective disease-modifying strategy.

382 Longitudinal and post-mortem studies from PD and AD cohorts show earlier onset of
383 cognitive decline and higher mortality rates with the presence of co-pathologies (Irwin et al., 2013,
384 Lim et al., 1999). Based on this, pure pathology is not common and may not be associated with
385 the cognitive impairment onset in these neurodegenerative diseases (Nelson et al., 2009, Wetering
386 et al., 2024). Here, we show that the presence of co-pathology results in enhanced neuronal loss,
387 specifically in the CA1 and CA3, regions of the hippocampus compared to single pathology
388 controls, correlating with region of enhanced pathology load in our model. While our dendritic
389 spine analysis at 6MPI implied some synaptic alterations in the hippocampus, it is possible that an
390 earlier timepoint may have captured more pronounced changes during the initial phase of synaptic
391 disintegration, prior to this marked neuronal loss. In the SNpc, however, dopaminergic neuronal

392 loss was prominent in the co-pathology model mice compared to the J20 mice, with no changes
393 between co-pathology mice and Tau or PFF single pathology animals. This is likely due to the
394 localization and abundance of the co-expression of these proteins in the hippocampus, suggesting
395 a region-specific interaction of pathology burden. These results highlight the need for further
396 mechanistic studies into the additive or synergistic roles of these pathologies on neurodegeneration
397 across multiple regions.

398 Microglial activation and the infiltration of T cells have been documented in response to
399 tau, Aβ, and α-syn individually in AD and PD (Chen and Yu, 2023, Hansen et al., 2018, Heneka
400 et al., 2015, Imamura et al., 2003, Zeng et al., 2024). However, studies implicating the role of
401 inflammation in driving neurodegeneration in a co-pathology model are lacking. Using this novel
402 co-pathology model, we show that the co-expression of these pathologies induces robust changes
403 in microglia, and enhanced infiltration of monocytes and T cells from the periphery indicating
404 neuroinflammation. Compared to single pathologies, the presence of co-pathologies resulted in
405 increased microglial cell count and activation status in the hippocampus and cortex. These changes
406 were not limited to microglia, as we observed a significant increase in infiltrating monocyte and
407 macrophages in areas with co-pathology burden. Our findings are consistent with recent work in
408 human postmortem tissue that compared microglia reactivity between mixed pathology
409 (DLB+AD) brains and pure pathology brains, showing higher levels of $CD68^+$, reactive microglia
410 in the hippocampus with mixed pathology (van Wetering et al., 2024). In our model, $CD68^+$
411 microglia were synergistically enhanced by the presence of co-pathology and showed heightened
412 proliferation and TLR2 expression, while $MHCII^+$ microglia decreased in number without
413 significant changes in expression of Ki67 or TLR2. Together, these findings suggest that the
414 presence of co-pathologies shifts the microglial response towards a more proliferative, phagocytic

415 phenotype, rather than a classic antigen-presenting role. Mechanistically, high deposition of
416 aggregated proteins may overwhelm phagocytic pathways within microglia, diverting resources
417 toward bulk debris clearance and away from peptide processing required for MHCII-mediated T
418 cell interactions. This microglial phenotype is consistent with the well-established profile of
419 disease-associated microglia (DAM), a pro-inflammatory state that is observed neurodegenerative
420 brain diseases (Friedman et al., 2018, Keren-Shaul et al., 2017, Krasemann et al., 2017). Future
421 work could determine whether the presence of co-pathology enhances DAM phenotypes in mice.
422 At 3MPI, we observed enhanced T cell responses compared to single pathologies in the
423 hippocampus and cortex and a synergistic expansion to Trm, marked by the expression of CD69
424 and CD103, which are key markers for tissue retention and local immune surveillance (Smolders
425 et al., 2018, Wakim et al., 2010). Trm have been shown to exacerbate disease through pro-
426 inflammatory cytokine release and cytolytic functions, which may modulate the response and
427 activation phenotypes of local microglia (Gate et al., 2020, Smolders et al., 2013) . The
428 accumulation of Trm in co-pathology brain implies their prolonged, antigen-responsive retention.
429 Future studies should further investigate the mechanisms by which co-pathologies drive the
430 accumulation of T cells in the CNS. Either by driving expression of tissue-residency ligands on
431 microglia for Trm retention or alternatively by promoting compensatory antigen presentation by
432 other CNS cells like border-associated macrophages, which have been shown promote T cell
433 infiltration more effectively than microglia in a neurodegenerative disease model (Schonhoff et
434 al., 2023). These findings suggest that chronic Trm-driven inflammation may represent a
435 converging mechanism of neurodegeneration regardless of the initiating proteinopathy. As such,
436 future depletion studies or modulation of Trm populations are necessary to determine whether co-

437 pathology driven Trm are disease driving or potentially neuroprotective by providing a local pool
438 of antigen experienced T cells in the CNS.

439 In conclusion, our findings collectively demonstrate that tau, Aβ and α-syn co-pathologies
440 enhance proteinopathy, synergistically enhance immune activation and subsequent
441 neurodegeneration. This synergy drives a robust immune response, shifting microglia towards a
442 CD68+ phagocytic phenotype, and significant Trm T cells in the hippocampus and cortex.
443 Additionally, this novel co-pathology model provides an important platform to further dissect how
444 co-pathologies shape neuroinflammatory responses in the CNS. Ultimately, our work strongly
445 supports the need for combinatorial therapeutic strategies that target multiple proteins and their
446 associated immune response, moving beyond single-target approaches to effectively alter disease
447 course.

448

449

450 # References

451 ALTENDORFER, B., UNGER, M. S., POUPARDIN, R., HOOG, A., ASSLABER, D., GRATZ,
452 I. K., MROWETZ, H., BENEDETTI, A., DE SOUSA, D. M. B., GREIL, R., EGLE, A.,
453 GATE, D., WYSS-CORAY, T. & AIGNER, L. 2022. Transcriptomic Profiling Identifies
454 CD8(+) T Cells in the Brain of Aged and Alzheimer's Disease Transgenic Mice as Tissue-
455 Resident Memory T Cells. *J Immunol,* 209**,** 1272-1285.
456 ANDORFER, C., KRESS, Y., ESPINOZA, M., DE SILVA, R., TUCKER, K. L., BARDE, Y. A.,
457 DUFF, K. & DAVIES, P. 2003. Hyperphosphorylation and aggregation of tau in mice
458 expressing normal human tau isoforms. *J Neurochem,* 86**,** 582-90.
459 BASSIL, F., BROWN, H. J., PATTABHIRAMAN, S., IWASYK, J. E., MAGHAMES, C. M.,
460 MEYMAND, E. S., COX, T. O., RIDDLE, D. M., ZHANG, B., TROJANOWSKI, J. Q. &
461 LEE, V. M. 2020. Amyloid-Beta (Aβ) Plaques Promote Seeding and Spreading of Alpha-
462 Synuclein and Tau in a Mouse Model of Lewy Body Disorders with Aβ Pathology. *Neuron,*
463 105**,** 260-275.e6.
464 BASSIL, F., MEYMAND, E. S., BROWN, H. J., XU, H., COX, T. O., PATTABHIRAMAN, S.,
465 MAGHAMES, C. M., WU, Q., ZHANG, B., TROJANOWSKI, J. Q. & LEE, V. M. 2021.
466 α-Synuclein modulates tau spreading in mouse brains. *J Exp Med,* 218.
467 BOURNE, J. N. & HARRIS, K. M. 2008. Balancing structure and function at hippocampal
468 dendritic spines. *Annu Rev Neurosci,* 31**,** 47-67.

469 BRAAK, H., DEL TREDICI, K., RÜB, U., DE VOS, R. A., JANSEN STEUR, E. N. & BRAAK,
470 E. 2003. Staging of brain pathology related to sporadic Parkinson's disease. *Neurobiol*
471 *Aging,* 24**,** 197-211.
472 BROCHARD, V., COMBADIERE, B., PRIGENT, A., LAOUAR, Y., PERRIN, A., BERAY-
473 BERTHAT, V., BONDUELLE, O., ALVAREZ-FISCHER, D., CALLEBERT, J.,
474 LAUNAY, J. M., DUYCKAERTS, C., FLAVELL, R. A., HIRSCH, E. C. & HUNOT, S.
475 2009. Infiltration of CD4+ lymphocytes into the brain contributes to neurodegeneration in
476 a mouse model of Parkinson disease. *J Clin Invest,* 119**,** 182-92.
477 BUCHMAN, A. S. & BENNETT, D. A. 2011. Loss of motor function in preclinical Alzheimer's
478 disease. *Expert Rev Neurother,* 11**,** 665-76.
479 BUSCHE, M. A., CHEN, X., HENNING, H. A., REICHWALD, J., STAUFENBIEL, M.,
480 SAKMANN, B. & KONNERTH, A. 2012. Critical role of soluble amyloid-β for early
481 hippocampal hyperactivity in a mouse model of Alzheimer's disease. *Proceedings of the*
482 *National Academy of Sciences,* 109**,** 8740-8745.
483 CHEN, X., FIRULYOVA, M., MANIS, M., HERZ, J., SMIRNOV, I., ALADYEVA, E., WANG,
484 C., BAO, X., FINN, M. B., HU, H., SHCHUKINA, I., KIM, M. W., YUEDE, C. M.,
485 KIPNIS, J., ARTYOMOV, M. N., ULRICH, J. D. & HOLTZMAN, D. M. 2023. Microglia-
486 mediated T cell infiltration drives neurodegeneration in tauopathy. *Nature,* 615**,** 668-677.
487 CHEN, Y. & YU, Y. 2023. Tau and neuroinflammation in Alzheimer's disease: interplay
488 mechanisms and clinical translation. *J Neuroinflammation,* 20**,** 165.
489 CLINTON, L. K., BLURTON-JONES, M., MYCZEK, K., TROJANOWSKI, J. Q. & LAFERLA,
490 F. M. 2010. Synergistic Interactions between Abeta, tau, and alpha-synuclein: acceleration
491 of neuropathology and cognitive decline. *J Neurosci,* 30**,** 7281-9.
492 COLOM-CADENA, M., GELPI, E., CHARIF, S., BELBIN, O., BLESA, R., MARTÍ, M. J.,
493 CLARIMÓN, J. & LLEÓ, A. 2013. Confluence of α-synuclein, tau, and β-amyloid
494 pathologies in dementia with Lewy bodies. *J Neuropathol Exp Neurol,* 72**,** 1203-12.
495 COMPTA, Y., PARKKINEN, L., KEMPSTER, P., SELIKHOVA, M., LASHLEY, T., HOLTON,
496 J. L., LEES, A. J. & REVESZ, T. 2014. The significance of α-synuclein, amyloid-β and tau
497 pathologies in Parkinson's disease progression and related dementia. *Neurodegener Dis,*
498 13**,** 154-6.
499 CORBIN-STEIN, N. J., CHILDERS, G. M., WEBSTER, J. M., ZANE, A., YANG, Y.-T.,
500 MUDIUM, N., GUPTA, R., MANFREDSSON, F. P., KORDOWER, J. H. & HARMS, A.
501 S. 2024. IFNγ drives neuroinflammation, demyelination, and neurodegeneration in a
502 mouse model of multiple system atrophy. *Acta Neuropathologica Communications,* 12**,** 11.
503 COUGHLIN, D., XIE, S. X., LIANG, M., WILLIAMS, A., PETERSON, C., WEINTRAUB, D.,
504 MCMILLAN, C. T., WOLK, D. A., AKHTAR, R. S., HURTIG, H. I., BRANCH
505 COSLETT, H., HAMILTON, R. H., SIDEROWF, A. D., DUDA, J. E., RASCOVSKY, K.,
506 LEE, E. B., LEE, V. M., GROSSMAN, M., TROJANOWSKI, J. Q. & IRWIN, D. J. 2019.
507 Cognitive and Pathological Influences of Tau Pathology in Lewy Body Disorders. *Ann*
508 *Neurol,* 85**,** 259-271.
509 DE CALIGNON, A., POLYDORO, M., SUÁREZ-CALVET, M., WILLIAM, C., ADAMOWICZ,
510 D. H., KOPEIKINA, K. J., PITSTICK, R., SAHARA, N., ASHE, K. H., CARLSON, G.
511 A., SPIRES-JONES, T. L. & HYMAN, B. T. 2012. Propagation of tau pathology in a model
512 of early Alzheimer's disease. *Neuron,* 73**,** 685-97.

513 DECRESSAC, M., MATTSSON, B., LUNDBLAD, M., WEIKOP, P. & BJÖRKLUND, A. 2012.
514 Progressive neurodegenerative and behavioural changes induced by AAV-mediated
515 overexpression of α-synuclein in midbrain dopamine neurons. *Neurobiol Dis,* 45**,** 939-53.
516 DEKOSKY, S. T. & SCHEFF, S. W. 1990. Synapse loss in frontal cortex biopsies in Alzheimer's
517 disease: correlation with cognitive severity. *Ann Neurol,* 27**,** 457-64.
518 DOUBLE, K. L. 2012. Neuronal vulnerability in Parkinson's disease. *Parkinsonism Relat Disord,*
519 18 Suppl 1**,** S52-4.
520 DUFF, K., ECKMAN, C., ZEHR, C., YU, X., PRADA, C. M., PEREZ-TUR, J., HUTTON, M.,
521 BUEE, L., HARIGAYA, Y., YAGER, D., MORGAN, D., GORDON, M. N., HOLCOMB,
522 L., REFOLO, L., ZENK, B., HARDY, J. & YOUNKIN, S. 1996. Increased amyloid-
523 beta42(43) in brains of mice expressing mutant presenilin 1. *Nature,* 383**,** 710-3.
524 ELABI, O., GACEB, A., CARLSSON, R., PADEL, T., SOYLU-KUCHARZ, R., CORTIJO, I., LI,
525 W., LI, J.-Y. & PAUL, G. 2021. Human α-synuclein overexpression in a mouse model of
526 Parkinson's disease leads to vascular pathology, blood brain barrier leakage and pericyte
527 activation. *Scientific Reports,* 11**,** 1120.
528 FERMAN, T. J., AOKI, N., CROOK, J. E., MURRAY, M. E., GRAFF-RADFORD, N. R., VAN
529 GERPEN, J. A., UITTI, R. J., WSZOLEK, Z. K., GRAFF-RADFORD, J., PEDRAZA, O.,
530 KANTARCI, K., BOEVE, B. F. & DICKSON, D. W. 2018. The limbic and neocortical
531 contribution of α-synuclein, tau, and amyloid β to disease duration in dementia with Lewy
532 bodies. *Alzheimers Dement,* 14**,** 330-339.
533 FERRETTI, M. T., MERLINI, M., SPÄNI, C., GERICKE, C., SCHWEIZER, N., ENZMANN,
534 G., ENGELHARDT, B., KULIC, L., SUTER, T. & NITSCH, R. M. 2016. T-cell brain
535 infiltration and immature antigen-presenting cells in transgenic models of Alzheimer's
536 disease-like cerebral amyloidosis. *Brain Behav Immun,* 54**,** 211-225.
537 FRANZMEIER, N., ROEMER-CASSIANO, S. N., BERNHARDT, A. M., DEHSARVI, A.,
538 DEWENTER, A., STEWARD, A., BIEL, D., FRONTZKOWSKI, L., ZHU, Z.,
539 GNÖRICH, J., PESCOLLER, J., WAGNER, F., HIRSCH, F., DE BRUIN, H.,
540 OSSENKOPPELE, R., PALLEIS, C., STRÜBING, F., SCHÖLL, M., LEVIN, J.,
541 BRENDEL, M. & HÖGLINGER, G. U. 2025. Alpha synuclein co-pathology is associated
542 with accelerated amyloid-driven tau accumulation in Alzheimer's disease. *Molecular*
543 *Neurodegeneration,* 20**,** 31.
544 FRIEDMAN, B. A., SRINIVASAN, K., AYALON, G., MEILANDT, W. J., LIN, H., HUNTLEY,
545 M. A., CAO, Y., LEE, S. H., HADDICK, P. C. G., NGU, H., MODRUSAN, Z., LARSON,
546 J. L., KAMINKER, J. S., VAN DER BRUG, M. P. & HANSEN, D. V. 2018. Diverse Brain
547 Myeloid Expression Profiles Reveal Distinct Microglial Activation States and Aspects of
548 Alzheimer's Disease Not Evident in Mouse Models. *Cell Rep,* 22**,** 832-847.
549 GALIANO-LANDEIRA, J., TORRA, A., VILA, M. & BOVÉ, J. 2020. CD8 T cell nigral
550 infiltration precedes synucleinopathy in early stages of Parkinson's disease. *Brain,* 143**,**
551 3717-3733.
552 GATE, D., SALIGRAMA, N., LEVENTHAL, O., YANG, A. C., UNGER, M. S., MIDDELDORP,
553 J., CHEN, K., LEHALLIER, B., CHANNAPPA, D., DE LOS SANTOS, M. B.,
554 MCBRIDE, A., PLUVINAGE, J., ELAHI, F., TAM, G. K., KIM, Y., GREICIUS, M.,
555 WAGNER, A. D., AIGNER, L., GALASKO, D. R., DAVIS, M. M. & WYSS-CORAY, T.
556 2020. Clonally expanded CD8 T cells patrol the cerebrospinal fluid in Alzheimer's disease.
557 *Nature,* 577**,** 399-404.

558 GATE, D., TAPP, E., LEVENTHAL, O., SHAHID, M., NONNINGER, T. J., YANG, A. C.,
559 STREMPFL, K., UNGER, M. S., FEHLMANN, T., OH, H., CHANNAPPA, D.,
560 HENDERSON, V. W., KELLER, A., AIGNER, L., GALASKO, D. R., DAVIS, M. M.,
561 POSTON, K. L. & WYSS-CORAY, T. 2021. CD4(+) T cells contribute to
562 neurodegeneration in Lewy body dementia. *Science,* 374**,** 868-874.
563 GIGUÈRE, N., BURKE NANNI, S. & TRUDEAU, L. E. 2018. On Cell Loss and Selective
564 Vulnerability of Neuronal Populations in Parkinson's Disease. *Front Neurol,* 9**,** 455.
565 GOEDERT, M. 1993. Tau protein and the neurofibrillary pathology of Alzheimer's disease. *Trends*
566 *Neurosci,* 16**,** 460-5.
567 GÓMEZ-BENITO, M., GRANADO, N., GARCÍA-SANZ, P., MICHEL, A., DUMOULIN, M. &
568 MORATALLA, R. 2020. Modeling Parkinson's Disease With the Alpha-Synuclein Protein.
569 *Front Pharmacol,* 11**,** 356.
570 GRAY, S. J., FOTI, S. B., SCHWARTZ, J. W., BACHABOINA, L., TAYLOR-BLAKE, B.,
571 COLEMAN, J., EHLERS, M. D., ZYLKA, M. J., MCCOWN, T. J. & SAMULSKI, R. J.
572 2011. Optimizing promoters for recombinant adeno-associated virus-mediated gene
573 expression in the peripheral and central nervous system using self-complementary vectors.
574 *Hum Gene Ther,* 22**,** 1143-53.
575 GREATHOUSE, K. M., BOROS, B. D., DESLAURIERS, J. F., HENDERSON, B. W., CURTIS,
576 K. A., GENTRY, E. G. & HERSKOWITZ, J. H. 2018. Distinct and complementary
577 functions of rho kinase isoforms ROCK1 and ROCK2 in prefrontal cortex structural
578 plasticity. *Brain Struct Funct,* 223**,** 4227-4241.
579 GREATHOUSE, K. M., HENDERSON, B. W., GENTRY, E. G. & HERSKOWITZ, J. H. 2019.
580 Fasudil or genetic depletion of ROCK1 or ROCK2 induces anxiety-like behaviors. *Behav*
581 *Brain Res,* 373**,** 112083.
582 GREFFARD, S., VERNY, M., BONNET, A. M., BEINIS, J. Y., GALLINARI, C., MEAUME, S.,
583 PIETTE, F., HAUW, J. J. & DUYCKAERTS, C. 2006. Motor score of the Unified
584 Parkinson Disease Rating Scale as a good predictor of Lewy body-associated neuronal loss
585 in the substantia nigra. *Arch Neurol,* 63**,** 584-8.
586 HAAGE, V. & DE JAGER, P. L. 2022. Neuroimmune contributions to Alzheimer's disease: a focus
587 on human data. *Mol Psychiatry,* 27**,** 3164-3181.
588 HANSEN, D. V., HANSON, J. E. & SHENG, M. 2018. Microglia in Alzheimer's disease. *J Cell*
589 *Biol,* 217**,** 459-472.
590 HARMS, A. S., THOME, A. D., YAN, Z., SCHONHOFF, A. M., WILLIAMS, G. P., LI, X., LIU,
591 Y., QIN, H., BENVENISTE, E. N. & STANDAERT, D. G. 2018. Peripheral monocyte
592 entry is required for alpha-Synuclein induced inflammation and Neurodegeneration in a
593 model of Parkinson disease. *Exp Neurol,* 300**,** 179-187.
594 HEFENDEHL, J. K., NEHER, J. J., SÜHS, R. B., KOHSAKA, S., SKODRAS, A. & JUCKER,
595 M. 2014. Homeostatic and injury-induced microglia behavior in the aging brain. *Aging*
596 *Cell,* 13**,** 60-9.
597 HENDERSON, B. W., GREATHOUSE, K. M., RAMDAS, R., WALKER, C. K., RAO, T. C.,
598 BACH, S. V., CURTIS, K. A., DAY, J. J., MATTHEYSES, A. L. & HERSKOWITZ, J. H.
599 2019. Pharmacologic inhibition of LIMK1 provides dendritic spine resilience against β-
600 amyloid. *Science Signaling,* 12**,** eaaw9318.
601 HENEKA, M. T., CARSON, M. J., EL KHOURY, J., LANDRETH, G. E., BROSSERON, F.,
602 FEINSTEIN, D. L., JACOBS, A. H., WYSS-CORAY, T., VITORICA, J., RANSOHOFF,
603 R. M., HERRUP, K., FRAUTSCHY, S. A., FINSEN, B., BROWN, G. C.,

VERKHRATSKY, A., YAMANAKA, K., KOISTINAHO, J., LATZ, E., HALLE, A., PETZOLD, G. C., TOWN, T., MORGAN, D., SHINOHARA, M. L., PERRY, V. H., HOLMES, C., BAZAN, N. G., BROOKS, D. J., HUNOT, S., JOSEPH, B., DEIGENDESCH, N., GARASCHUK, O., BODDEKE, E., DINARELLO, C. A., BREITNER, J. C., COLE, G. M., GOLENBOCK, D. T. & KUMMER, M. P. 2015. Neuroinflammation in Alzheimer's disease. *Lancet Neurol,* 14**,** 388-405.

HENEKA, M. T., KUMMER, M. P., STUTZ, A., DELEKATE, A., SCHWARTZ, S., VIEIRA-SAECKER, A., GRIEP, A., AXT, D., REMUS, A., TZENG, T. C., GELPI, E., HALLE, A., KORTE, M., LATZ, E. & GOLENBOCK, D. T. 2013. NLRP3 is activated in Alzheimer's disease and contributes to pathology in APP/PS1 mice. *Nature,* 493**,** 674-8.

IMAMURA, K., HISHIKAWA, N., SAWADA, M., NAGATSU, T., YOSHIDA, M. & HASHIZUME, Y. 2003. Distribution of major histocompatibility complex class II-positive microglia and cytokine profile of Parkinson's disease brains. *Acta Neuropathol,* 106**,** 518-26.

IRWIN, D. J., GROSSMAN, M., WEINTRAUB, D., HURTIG, H. I., DUDA, J. E., XIE, S. X., LEE, E. B., VAN DEERLIN, V. M., LOPEZ, O. L., KOFLER, J. K., NELSON, P. T., JICHA, G. A., WOLTJER, R., QUINN, J. F., KAYE, J., LEVERENZ, J. B., TSUANG, D., LONGFELLOW, K., YEAROUT, D., KUKULL, W., KEENE, C. D., MONTINE, T. J., ZABETIAN, C. P. & TROJANOWSKI, J. Q. 2017. Neuropathological and genetic correlates of survival and dementia onset in synucleinopathies: a retrospective analysis. *Lancet Neurol,* 16**,** 55-65.

IRWIN, D. J., LEE, V. M. & TROJANOWSKI, J. Q. 2013. Parkinson's disease dementia: convergence of alpha-synuclein, tau and amyloid-beta pathologies. *Nat Rev Neurosci,* 14**,** 626-36.

IRWIN, D. J., XIE, S. X., COUGHLIN, D., NEVLER, N., AKHTAR, R. S., MCMILLAN, C. T., LEE, E. B., WOLK, D. A., WEINTRAUB, D., CHEN-PLOTKIN, A., DUDA, J. E., SPINDLER, M., SIDEROWF, A., HURTIG, H. I., SHAW, L. M., GROSSMAN, M. & TROJANOWSKI, J. Q. 2018. CSF tau and β-amyloid predict cerebral synucleinopathy in autopsied Lewy body disorders. *Neurology,* 90**,** e1038-e1046.

ITAGAKI, S., MCGEER, P. L. & AKIYAMA, H. 1988. Presence of T-cytotoxic suppressor and leucocyte common antigen positive cells in Alzheimer's disease brain tissue. *Neurosci Lett,* 91**,** 259-64.

JELLINGER, K. A. 2002. Alzheimer disease and cerebrovascular pathology: an update. *J Neural Transm (Vienna),* 109**,** 813-36.

JELLINGER, K. A. 2003. Alpha-synuclein pathology in Parkinson's and Alzheimer's disease brain: incidence and topographic distribution--a pilot study. *Acta Neuropathol,* 106**,** 191-201.

JELLINGER, K. A. 2020. Neuropathological assessment of the Alzheimer spectrum. *J Neural Transm (Vienna),* 127**,** 1229-1256.

JOACHIM, C. L. & SELKOE, D. J. 1989. Amyloid protein in Alzheimer's disease. *J Gerontol,* 44**,** B77-82.

KARIKARI, A. A., MCFLEDER, R. L., RIBECHINI, E., BLUM, R., BRUTTEL, V., KNORR, S., GEHMEYR, M., VOLKMANN, J., BROTCHIE, J. M., AHSAN, F., HAACK, B., MONORANU, C. M., KEBER, U., YEGHIAZARYAN, R., PAGENSTECHER, A., HECKEL, T., BISCHLER, T., WISCHHUSEN, J., KOPRICH, J. B., LUTZ, M. B. & IP,

C. W. 2022. Neurodegeneration by α-synuclein-specific T cells in AAV-A53T-α-synuclein Parkinson's disease mice. *Brain Behav Immun,* 101**,** 194-210.

KARPENKO, M. N., VASILISHINA, A. A., GROMOVA, E. A., MURUZHEVA, Z. M., MILIUKHINA, I. V. & BERNADOTTE, A. 2018. Interleukin-1β, interleukin-1 receptor antagonist, interleukin-6, interleukin-10, and tumor necrosis factor-α levels in CSF and serum in relation to the clinical diversity of Parkinson's disease. *Cell Immunol,* 327**,** 77-82.

KEREN-SHAUL, H., SPINRAD, A., WEINER, A., MATCOVITCH-NATAN, O., DVIR-SZTERNFELD, R., ULLAND, T. K., DAVID, E., BARUCH, K., LARA-ASTAISO, D., TOTH, B., ITZKOVITZ, S., COLONNA, M., SCHWARTZ, M. & AMIT, I. 2017. A Unique Microglia Type Associated with Restricting Development of Alzheimer's Disease. *Cell,* 169**,** 1276-1290.e17.

KIMURA, K., NISHIGORI, R., HAMATANI, M., SAWAMURA, M., ASHIDA, S., FUJII, C., TAKATA, M., LIN, Y., SATO, W., OKAMOTO, T., KUZUYA, A., TAKAHASHI, R., YAMAMURA, T. & KONDO, T. 2024. Resident Memory-like CD8(+) T Cells Are Involved in Chronic Inflammatory and Neurodegenerative Diseases in the CNS. *Neurol Neuroimmunol Neuroinflamm,* 11.

KNOBLOCH, M. & MANSUY, I. M. 2008. Dendritic spine loss and synaptic alterations in Alzheimer's disease. *Mol Neurobiol,* 37**,** 73-82.

KOTZBAUER, P. T., CAIRNS, N. J., CAMPBELL, M. C., WILLIS, A. W., RACETTE, B. A., TABBAL, S. D. & PERLMUTTER, J. S. 2012. Pathologic accumulation of α-synuclein and Aβ in Parkinson disease patients with dementia. *Arch Neurol,* 69**,** 1326-31.

KOULI, A., CAMACHO, M., ALLINSON, K. & WILLIAMS-GRAY, C. H. 2020. Neuroinflammation and protein pathology in Parkinson's disease dementia. *Acta Neuropathol Commun,* 8**,** 211.

KRASEMANN, S., MADORE, C., CIALIC, R., BAUFELD, C., CALCAGNO, N., EL FATIMY, R., BECKERS, L., O'LOUGHLIN, E., XU, Y., FANEK, Z., GRECO, D. J., SMITH, S. T., TWEET, G., HUMULOCK, Z., ZRZAVY, T., CONDE-SANROMAN, P., GACIAS, M., WENG, Z., CHEN, H., TJON, E., MAZAHERI, F., HARTMANN, K., MADI, A., ULRICH, J. D., GLATZEL, M., WORTHMANN, A., HEEREN, J., BUDNIK, B., LEMERE, C., IKEZU, T., HEPPNER, F. L., LITVAK, V., HOLTZMAN, D. M., LASSMANN, H., WEINER, H. L., OCHANDO, J., HAASS, C. & BUTOVSKY, O. 2017. The TREM2-APOE Pathway Drives the Transcriptional Phenotype of Dysfunctional Microglia in Neurodegenerative Diseases. *Immunity,* 47**,** 566-581.e9.

KRAYBILL, M. L., LARSON, E. B., TSUANG, D. W., TERI, L., MCCORMICK, W. C., BOWEN, J. D., KUKULL, W. A., LEVERENZ, J. B. & CHERRIER, M. M. 2005. Cognitive differences in dementia patients with autopsy-verified AD, Lewy body pathology, or both. *Neurology,* 64**,** 2069-73.

LEWIS, J., DICKSON, D. W., LIN, W. L., CHISHOLM, L., CORRAL, A., JONES, G., YEN, S. H., SAHARA, N., SKIPPER, L., YAGER, D., ECKMAN, C., HARDY, J., HUTTON, M. & MCGOWAN, E. 2001. Enhanced neurofibrillary degeneration in transgenic mice expressing mutant tau and APP. *Science,* 293**,** 1487-91.

LEWIS, J., MCGOWAN, E., ROCKWOOD, J., MELROSE, H., NACHARAJU, P., VAN SLEGTENHORST, M., GWINN-HARDY, K., PAUL MURPHY, M., BAKER, M., YU, X., DUFF, K., HARDY, J., CORRAL, A., LIN, W. L., YEN, S. H., DICKSON, D. W., DAVIES, P. & HUTTON, M. 2000. Neurofibrillary tangles, amyotrophy and progressive motor disturbance in mice expressing mutant (P301L) tau protein. *Nat Genet,* 25**,** 402-5.

LIM, A., TSUANG, D., KUKULL, W., NOCHLIN, D., LEVERENZ, J., MCCORMICK, W., BOWEN, J., TERI, L., THOMPSON, J., PESKIND, E. R., RASKIND, M. & LARSON, E. B. 1999. Clinico-neuropathological correlation of Alzheimer's disease in a community-based case series. *J Am Geriatr Soc,* 47**,** 564-9.

LUK, K. C., SONG, C., O'BRIEN, P., STIEBER, A., BRANCH, J. R., BRUNDEN, K. R., TROJANOWSKI, J. Q. & LEE, V. M. 2009. Exogenous alpha-synuclein fibrils seed the formation of Lewy body-like intracellular inclusions in cultured cells. *Proc Natl Acad Sci U S A,* 106**,** 20051-6.

MA, M., PARYANI, F., JAKUBIAK, K., XIA, S., ANTOKU, S., KANNAN, A., LEE, J., MADDEN, N., SENTHIL KUMAR, S., LI, J., CHEN, D., HARGUS, G., MAHAJAN, A., FLOWERS, X., HARMS, A. S., SULZER, D., GOLDMAN, J. E., SIMS, P. A. & AL-DALAHMAH, O. 2025. The spatial landscape of glial pathology and T cell response in Parkinson's disease substantia nigra. *Nature Communications,* 16**,** 7146.

MAK, E., REID, R. I., PRZYBELSKI, S. A., LESNICK, T. G., SCHWARZ, C. G., SENJEM, M. L., RAGHAVAN, S., VEMURI, P., JACK, C. R., JR., MIN, H. K., JAIN, M. K., MIYAGAWA, T., FORSBERG, L. K., FIELDS, J. A., SAVICA, R., GRAFF-RADFORD, J., JONES, D. T., BOTHA, H., ST LOUIS, E. K., KNOPMAN, D. S., RAMANAN, V. K., DICKSON, D. W., GRAFF-RADFORD, N. R., FERMAN, T. J., PETERSEN, R. C., LOWE, V. J., BOEVE, B. F., O'BRIEN, J. T. & KANTARCI, K. 2024. Influences of amyloid-β and tau on white matter neurite alterations in dementia with Lewy bodies. *NPJ Parkinsons Dis,* 10**,** 76.

MALEK-AHMADI, M., BEACH, T. G., ZAMRINI, E., ADLER, C. H., SABBAGH, M. N., SHILL, H. A., JACOBSON, S. A., BELDEN, C. M., CASELLI, R. J., WOODRUFF, B. K., RAPSCAK, S. Z., AHERN, G. L., SHI, J., CAVINESS, J. N., DRIVER-DUNCKLEY, E., MEHTA, S. H., SHPRECHER, D. R., SPANN, B. M., TARIOT, P., DAVIS, K. J., LONG, K. E., NICHOLSON, L. R., INTORCIA, A., GLASS, M. J., WALKER, J. E., CALLAN, M., CURRY, J., CUTLER, B., OLIVER, J., ARCE, R., WALKER, D. G., LUE, L. F., SERRANO, G. E., SUE, L. I., CHEN, K. & REIMAN, E. M. 2019. Faster cognitive decline in dementia due to Alzheimer disease with clinically undiagnosed Lewy body disease. *PLoS One,* 14**,** e0217566.

MAPHIS, N., XU, G., KOKIKO-COCHRAN, O. N., JIANG, S., CARDONA, A., RANSOHOFF, R. M., LAMB, B. T. & BHASKAR, K. 2015. Reactive microglia drive tau pathology and contribute to the spreading of pathological tau in the brain. *Brain,* 138**,** 1738-55.

MERLINI, M., KIRABALI, T., KULIC, L., NITSCH, R. M. & FERRETTI, M. T. 2018. Extravascular CD3+ T Cells in Brains of Alzheimer Disease Patients Correlate with Tau but Not with Amyloid Pathology: An Immunohistochemical Study. *Neurodegener Dis,* 18**,** 49-56.

MRDJEN, D., FOX, E. J., BUKHARI, S. A., MONTINE, K. S., BENDALL, S. C. & MONTINE, T. J. 2019. The basis of cellular and regional vulnerability in Alzheimer's disease. *Acta Neuropathol,* 138**,** 729-749.

MUCKE, L., MASLIAH, E., YU, G. Q., MALLORY, M., ROCKENSTEIN, E. M., TATSUNO, G., HU, K., KHOLODENKO, D., JOHNSON-WOOD, K. & MCCONLOGUE, L. 2000. High-level neuronal expression of abeta 1-42 in wild-type human amyloid protein precursor transgenic mice: synaptotoxicity without plaque formation. *J Neurosci,* 20**,** 4050-8.

NELSON, P. T., BRAAK, H. & MARKESBERY, W. R. 2009. Neuropathology and cognitive impairment in Alzheimer disease: a complex but coherent relationship. *J Neuropathol Exp Neurol,* 68**,** 1-14.

OLAJIDE, O. J., SUVANTO, M. E. & CHAPMAN, C. A. 2021. Molecular mechanisms of neurodegeneration in the entorhinal cortex that underlie its selective vulnerability during the pathogenesis of Alzheimer's disease. *Biol Open,* 10.

PAMPUSCENKO, K., MORKUNIENE, R., KRASAUSKAS, L., SMIRNOVAS, V., BROWN, G. C. & BORUTAITE, V. 2023. Extracellular tau stimulates phagocytosis of living neurons by activated microglia via Toll-like 4 receptor-NLRP3 inflammasome-caspase-1 signalling axis. *Sci Rep,* 13**,** 10813.

PINTO-COSTA, R., HARBACHOVA, E., LA VITOLA, P. & DI MONTE, D. A. 2023. Overexpression-Induced α-Synuclein Brain Spreading. *Neurotherapeutics,* 20**,** 83-96.

RIES, M. & SASTRE, M. 2016. Mechanisms of Aβ Clearance and Degradation by Glial Cells. *Front Aging Neurosci,* 8**,** 160.

ROBINSON, J. L., LEE, E. B., XIE, S. X., RENNERT, L., SUH, E., BREDENBERG, C., CASWELL, C., VAN DEERLIN, V. M., YAN, N., YOUSEF, A., HURTIG, H. I., SIDEROWF, A., GROSSMAN, M., MCMILLAN, C. T., MILLER, B., DUDA, J. E., IRWIN, D. J., WOLK, D., ELMAN, L., MCCLUSKEY, L., CHEN-PLOTKIN, A., WEINTRAUB, D., ARNOLD, S. E., BRETTSCHNEIDER, J., LEE, V. M. & TROJANOWSKI, J. Q. 2018. Neurodegenerative disease concomitant proteinopathies are prevalent, age-related and APOE4-associated. *Brain,* 141**,** 2181-2193.

ROGERS, J., LUBER-NAROD, J., STYREN, S. D. & CIVIN, W. H. 1988. Expression of immune system-associated antigens by cells of the human central nervous system: relationship to the pathology of Alzheimer's disease. *Neurobiol Aging,* 9**,** 339-49.

SANDOVAL, I. M., KUHN, N. M. & MANFREDSSON, F. P. 2019. Multimodal Production of Adeno-Associated Virus. *Methods Mol Biol,* 1937**,** 101-124.

SCHNEIDER, J. A., ARVANITAKIS, Z., BANG, W. & BENNETT, D. A. 2007. Mixed brain pathologies account for most dementia cases in community-dwelling older persons. *Neurology,* 69**,** 2197-204.

SCHONHOFF, A. M., FIGGE, D. A., WILLIAMS, G. P., JURKUVENAITE, A., GALLUPS, N. J., CHILDERS, G. M., WEBSTER, J. M., STANDAERT, D. G., GOLDMAN, J. E. & HARMS, A. S. 2023. Border-associated macrophages mediate the neuroinflammatory response in an alpha-synuclein model of Parkinson disease. *Nature Communications,* 14**,** 3754.

SELKOE, D. J. 2002. Alzheimer's disease is a synaptic failure. *Science,* 298**,** 789-91.

SENGUPTA, U. & KAYED, R. 2022. Amyloid β, Tau, and α-Synuclein aggregates in the pathogenesis, prognosis, and therapeutics for neurodegenerative diseases. *Prog Neurobiol,* 214**,** 102270.

SHABIR, O., SHARP, P., REBOLLAR, M. A., BOORMAN, L., HOWARTH, C., WHARTON, S. B., FRANCIS, S. E. & BERWICK, J. 2020. Enhanced Cerebral Blood Volume under Normobaric Hyperoxia in the J20-hAPP Mouse Model of Alzheimer’s Disease. *Scientific Reports,* 10**,** 7518.

SHIPTON, O. A., LEITZ, J. R., DWORZAK, J., ACTON, C. E., TUNBRIDGE, E. M., DENK, F., DAWSON, H. N., VITEK, M. P., WADE-MARTINS, R., PAULSEN, O. & VARGAS-CABALLERO, M. 2011. Tau protein is required for amyloid {beta}-induced impairment of hippocampal long-term potentiation. *J Neurosci,* 31**,** 1688-92.

786 SMOLDERS, J., HEUTINCK, K. M., FRANSEN, N. L., REMMERSWAAL, E. B. M.,
787 HOMBRINK, P., TEN BERGE, I. J. M., VAN LIER, R. A. W., HUITINGA, I. &
788 HAMANN, J. 2018. Tissue-resident memory T cells populate the human brain. *Nat*
789 *Commun,* 9**,** 4593.
790 SMOLDERS, J., REMMERSWAAL, E. B., SCHUURMAN, K. G., MELIEF, J., VAN EDEN, C.
791 G., VAN LIER, R. A., HUITINGA, I. & HAMANN, J. 2013. Characteristics of
792 differentiated CD8(+) and CD4 (+) T cells present in the human brain. *Acta Neuropathol,*
793 126**,** 525-35.
794 SPILLANTINI, M. G., SCHMIDT, M. L., LEE, V. M., TROJANOWSKI, J. Q., JAKES, R. &
795 GOEDERT, M. 1997. Alpha-synuclein in Lewy bodies. *Nature,* 388**,** 839-40.
796 SPIRES-JONES, T. L., ATTEMS, J. & THAL, D. R. 2017. Interactions of pathological proteins in
797 neurodegenerative diseases. *Acta Neuropathol,* 134**,** 187-205.
798 SPIRES-JONES, T. L. & HYMAN, B. T. 2014. The intersection of amyloid beta and tau at
799 synapses in Alzheimer's disease. *Neuron,* 82**,** 756-71.
800 SU, W., SARAVIA, J., RISCH, I., RANKIN, S., GUY, C., CHAPMAN, N. M., SHI, H., SUN, Y.,
801 KC, A., LI, W., HUANG, H., LIM, S. A., HU, H., WANG, Y., LIU, D., JIAO, Y., CHEN,
802 P. C., SOLIMAN, H., YAN, K. K., ZHANG, J., VOGEL, P., LIU, X., SERRANO, G. E.,
803 BEACH, T. G., YU, J., PENG, J. & CHI, H. 2023. CXCR6 orchestrates brain CD8(+) T
804 cell residency and limits mouse Alzheimer's disease pathology. *Nat Immunol,* 24**,** 1735-
805 1747.
806 SULZER, D., ALCALAY, R. N., GARRETTI, F., COTE, L., KANTER, E., AGIN-LIEBES, J.,
807 LIONG, C., MCMURTREY, C., HILDEBRAND, W. H., MAO, X., DAWSON, V. L.,
808 DAWSON, T. M., OSEROFF, C., PHAM, J., SIDNEY, J., DILLON, M. B., CARPENTER,
809 C., WEISKOPF, D., PHILLIPS, E., MALLAL, S., PETERS, B., FRAZIER, A.,
810 LINDESTAM ARLEHAMN, C. S. & SETTE, A. 2017. T cells from patients with
811 Parkinson's disease recognize alpha-synuclein peptides. *Nature,* 546**,** 656-661.
812 TOGO, T., AKIYAMA, H., ISEKI, E., KONDO, H., IKEDA, K., KATO, M., ODA, T.,
813 TSUCHIYA, K. & KOSAKA, K. 2002. Occurrence of T cells in the brain of Alzheimer's
814 disease and other neurological diseases. *J Neuroimmunol,* 124**,** 83-92.
815 TWOHIG, D. & NIELSEN, H. M. 2019. α-synuclein in the pathophysiology of Alzheimer's
816 disease. *Mol Neurodegener,* 14**,** 23.
817 VAN DER GAAG, B. L., DESHAYES, N. A. C., BREVE, J. J. P., BOL, J., JONKER, A. J.,
818 HOOZEMANS, J. J. M., COURADE, J. P. & VAN DE BERG, W. D. J. 2024. Distinct tau
819 and alpha-synuclein molecular signatures in Alzheimer's disease with and without Lewy
820 bodies and Parkinson's disease with dementia. *Acta Neuropathol,* 147**,** 14.
821 VAN WETERING, J., GEUT, H., BOL, J. J., GALIS, Y., TIMMERMANS, E., TWISK, J. W. R.,
822 HEPP, D. H., MORELLA, M. L., PIHLSTROM, L., LEMSTRA, A. W., ROZEMULLER,
823 A. J. M., JONKMAN, L. E. & VAN DE BERG, W. D. J. 2024. Neuroinflammation is
824 associated with Alzheimer's disease co-pathology in dementia with Lewy bodies. *Acta*
825 *Neuropathol Commun,* 12**,** 73.
826 VOLPICELLI-DALEY, L. A., LUK, K. C. & LEE, V. M. 2014. Addition of exogenous α-synuclein
827 preformed fibrils to primary neuronal cultures to seed recruitment of endogenous α-
828 synuclein to Lewy body and Lewy neurite-like aggregates. *Nat Protoc,* 9**,** 2135-46.
829 WAKIM, L. M., WOODWARD-DAVIS, A. & BEVAN, M. J. 2010. Memory T cells persisting
830 within the brain after local infection show functional adaptations to their tissue of
831 residence. *Proc Natl Acad Sci U S A,* 107**,** 17872-9.

832 WANG, P., YAO, L., LUO, M., ZHOU, W., JIN, X., XU, Z., YAN, S., LI, Y., XU, C., CHENG, R.,
833 HUANG, Y., LIN, X., MA, K., CAO, H., LIU, H., XUE, G., HAN, F., NIE, H. & JIANG,
834 Q. 2021. Single-cell transcriptome and TCR profiling reveal activated and expanded T cell
835 populations in Parkinson's disease. *Cell Discov,* 7**,** 52.
836 WETERING, J. V., GEUT, H., BOL, J. J., GALIS, Y., TIMMERMANS, E., TWISK, J. W. R.,
837 HEPP, D. H., MORELLA, M. L., PIHLSTROM, L., LEMSTRA, A. W., ROZEMULLER,
838 A. J. M., JONKMAN, L. E. & VAN DE BERG, W. D. J. 2024. Neuroinflammation is
839 associated with Alzheimer's disease co-pathology in dementia with Lewy bodies. *Acta*
840 *Neuropathologica Communications,* 12**,** 73.
841 WILLIAMS, G. P., SCHONHOFF, A. M., JURKUVENAITE, A., THOME, A. D., STANDAERT,
842 D. G. & HARMS, A. S. 2018. Targeting of the class II transactivator attenuates
843 inflammation and neurodegeneration in an alpha-synuclein model of Parkinson's disease.
844 *J Neuroinflammation,* 15**,** 244.
845 YAMAKAWA, M. & REXACH, J. E. 2024. Cell States and Interactions of CD8 T Cells and
846 Disease-Enriched Microglia in Human Brains with Alzheimer's Disease. *Biomedicines,* 12.
847 YAN, Z., YANG, W., WEI, H., DEAN, M. N., STANDAERT, D. G., CUTTER, G. R.,
848 BENVENISTE, E. N. & QIN, H. 2021. Dysregulation of the Adaptive Immune System in
849 Patients With Early-Stage Parkinson Disease. *Neurol Neuroimmunol Neuroinflamm,* 8.
850 ZENG, J., LIAO, Z., YANG, H., WANG, Q., WU, Z., HUA, F. & ZHOU, Z. 2024. T cell infiltration
851 mediates neurodegeneration and cognitive decline in Alzheimer's disease. *Neurobiol Dis,*
852 193**,** 106461.
853 ZHAO, Y., WU, X., LI, X., JIANG, L. L., GUI, X., LIU, Y., SUN, Y., ZHU, B., PIÑA-CRESPO,
854 J. C., ZHANG, M., ZHANG, N., CHEN, X., BU, G., AN, Z., HUANG, T. Y. & XU, H.
855 2018. TREM2 Is a Receptor for β-Amyloid that Mediates Microglial Function. *Neuron,* 97**,**
856 1023-1031.e7.
857

858 # Figures

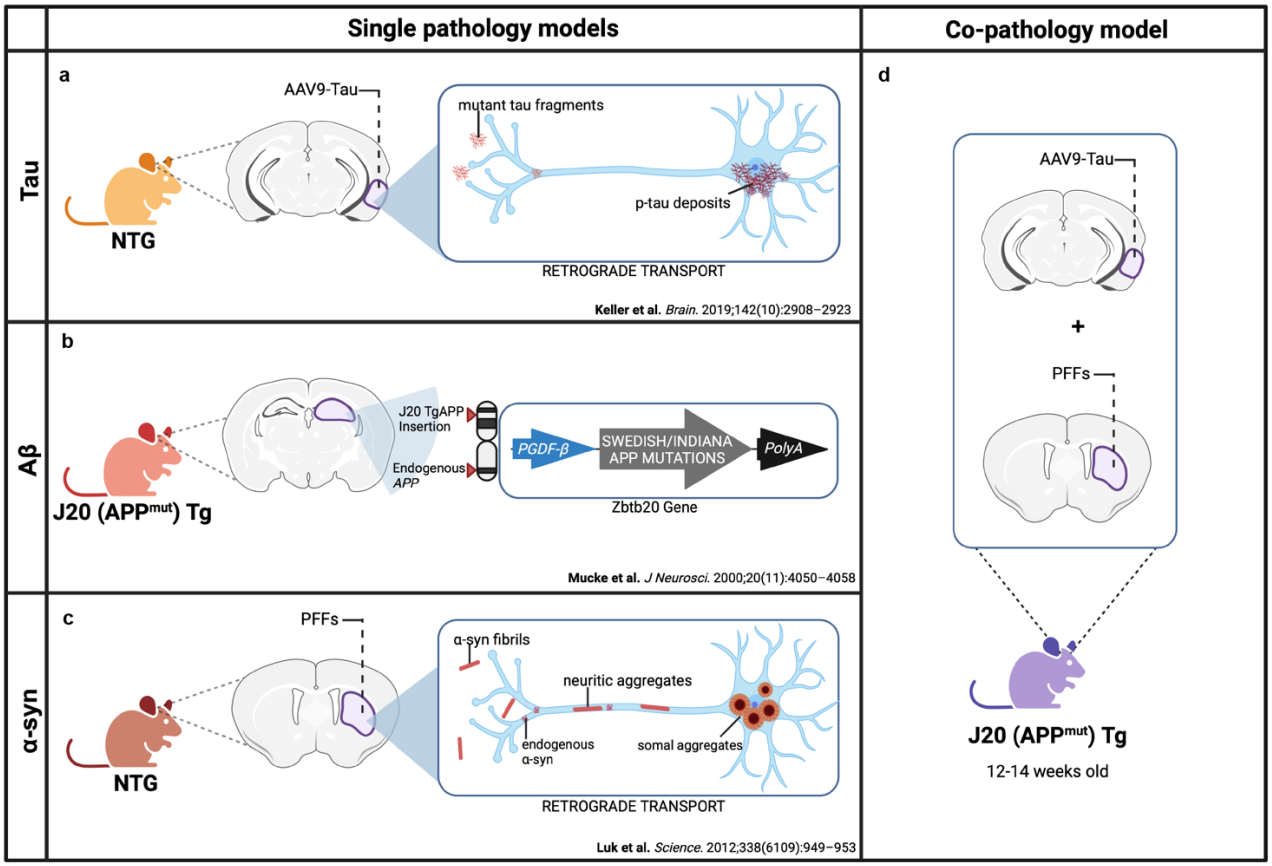

Figure 1. Strategy for creating co-pathology mouse model. At 12-14 weeks old, non-transgenic (NTG) wild-type or J20 APP mutant (APP^{mut}) transgenic (Tg) age-matched males and females are used to induce either single pathology controls or the co-pathology model *in vivo*. (a) For tau single pathology controls, NTG mice received injections of 2μL of 3.2E12 vg/mL AAV9-Tau into the entorhinal cortex. This viral overexpression of mutant tau results in the accumulation of phosphorylated tau (p-tau) in the cell body via retrograde transport. (b) For Aβ pathology, J20 Tg mice expressing human APP with Swedish and Indiana mutations under the PGDF-β promoter were used. These mice develop Aβ plaques due to overproduction and deposition of Aβ. (c) For α-syn pathology in the PFF single pathology control, NTG mice were injected with 2μL of 5μg α-syn PFFs into the striatum. Fibrils deposited into the brain will interact with endogenous α-syn within the neurons to form neuritic and somal aggregates. (d) For the co-pathology model, J20 Tg

871 mice received both AAV9-Tau and α-syn PFFs into the entorhinal cortex and striatum,
872 respectively, to simultaneously induce the expression of Aβ, tau and α-syn the brain.

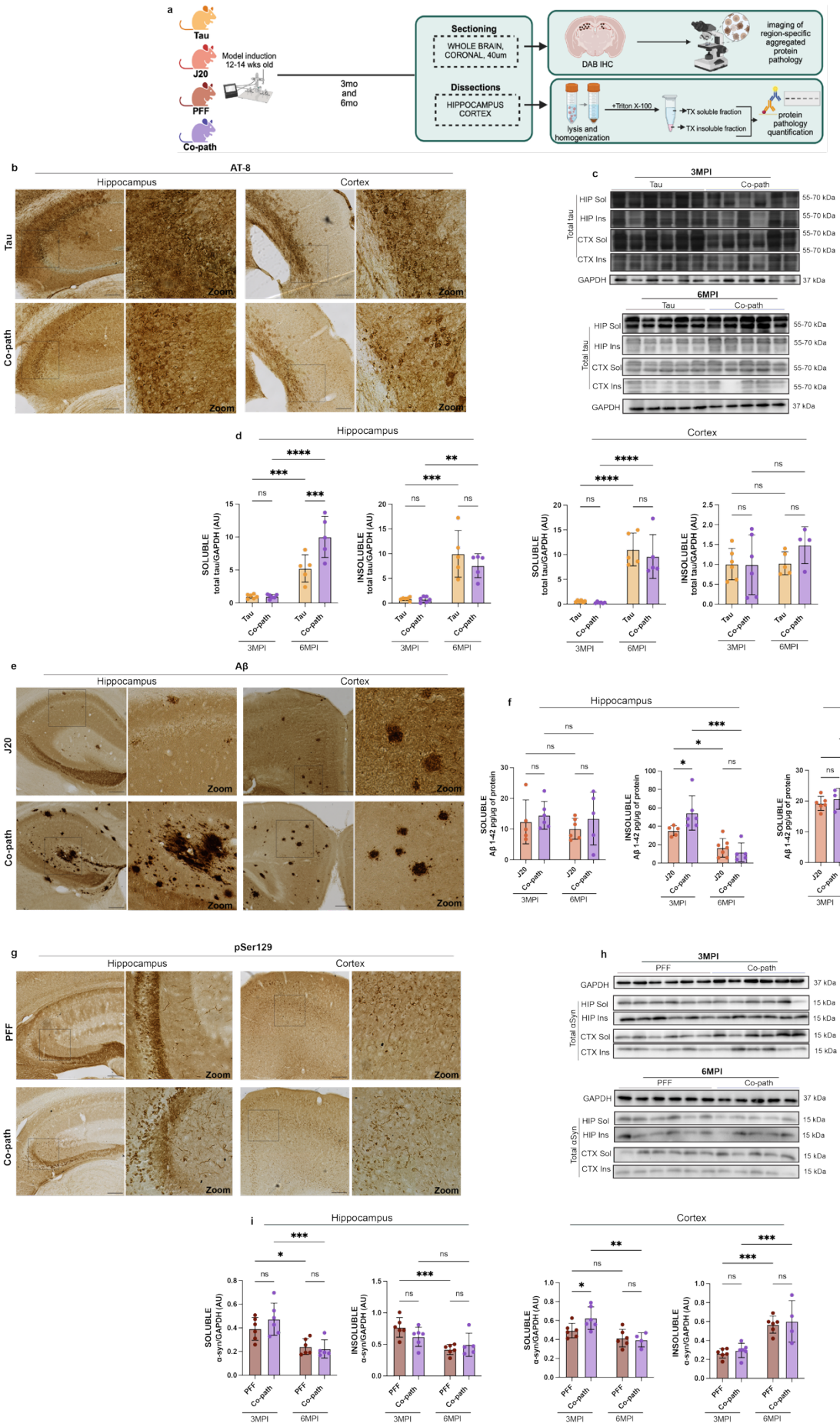
a
Tau
J20
PFF
Co-path
Model induction 12-14 wks old
3mo and 6mo
Sectioning
WHOLE BRAIN, CORONAL, 40um
Dissections
HIPPOCAMPUS CORTEX
DAB IHC
imaging of region-specific aggregated protein pathology
lysis and homogenization
+Triton X-100
TX soluble fraction
TX insoluble fraction
protein pathology quantification
b
AT-8
Hippocampus
Cortex
Tau
Co-path
Zoom
c
3MPI
6MPI
Tau
Co-path
Total tau
HIP Sol
HIP Ins
CTX Sol
CTX Ins
GAPDH
55-70 kDa
37 kDa
d
Hippocampus
Cortex
SOLUBLE total tau/GAPDH (AU)
INSOLUBLE total tau/GAPDH (AU)
3MPI
6MPI
e
Aβ
J20
f
SOLUBLE Aβ 1-42 pg/µg of protein
INSOLUBLE Aβ 1-42 pg/µg of protein
g
pSer129
PFF
h
Total αSyn
15 kDa
i
SOLUBLE α-syn/GAPDH (AU)
INSOLUBLE α-syn/GAPDH (AU)

874 **Figure 2. The presence of co-pathology enhances $A\beta_{1-42}$ and α-syn protein levels in the**
875 **hippocampus and cortex at 3MPI and total tau protein in the hippocampus at 6MPI.** (a) 12–
876 14-week-old animals were induced with either single pathologies or co-pathologies. At 3MPI and
877 6MPI, mice were sacrificed and brains processed for IHC or biochemical analysis of protein levels.
878 (b) AT-8/pTau-positive neurons (DAB+, brown) in the hippocampus and cortex of tau single
879 pathology and co-pathology brains. (c) Representative immunoblot of total tau and GAPDH levels
880 from 3MPI and 6MPI co-pathology and Tau single pathology brains. Blots are cropped from
881 original images found in Source Data. (d) Quantification of tau protein levels normalized to
882 GAPDH levels in Triton X-100 (TX)-soluble and TX-insoluble hippocampus and cortical samples
883 from Tau single pathology and co-pathology mice at 3MPI and 6MPI. (e) Aβ-positive plaques
884 (DAB+, brown) expressed within the hippocampus and cortex of J20 single pathology (Aβ) and
885 co-pathology brains. (f) ELISA was used to quantify $A\beta_{1-42}$ levels in the brains of 3MPI and 6MPI
886 J20 single pathology and co-pathology mice. TX soluble and insoluble fractions of 3MPI and 6MPI
887 co-pathology and single pathology hippocampal and cortical tissue were used. (g) pSer129-
888 positive inclusions in the hippocampus and cortex of PFF only (α-syn) and co-pathology brains.
889 (h) Representative immunoblot of total α-syn and GAPDH. Blots are cropped from original images
890 found in Source Data. (i) Quantification of synuclein protein levels normalized to GAPDH levels
891 in TX-soluble and TX-insoluble hippocampus and cortical samples from PFF single pathology and
892 co-pathology mice at 3MPI and 6MPI. All images taken at 10X or 20X for zooms, scale bars =
893 100μm. Analyzed using Welch's t-test. *$p<0.05$, **$p<0.01$, ***$p<0.001$, ****$p<0.0001$. n=5-6
894 animals per group, both males and females used.
895
896

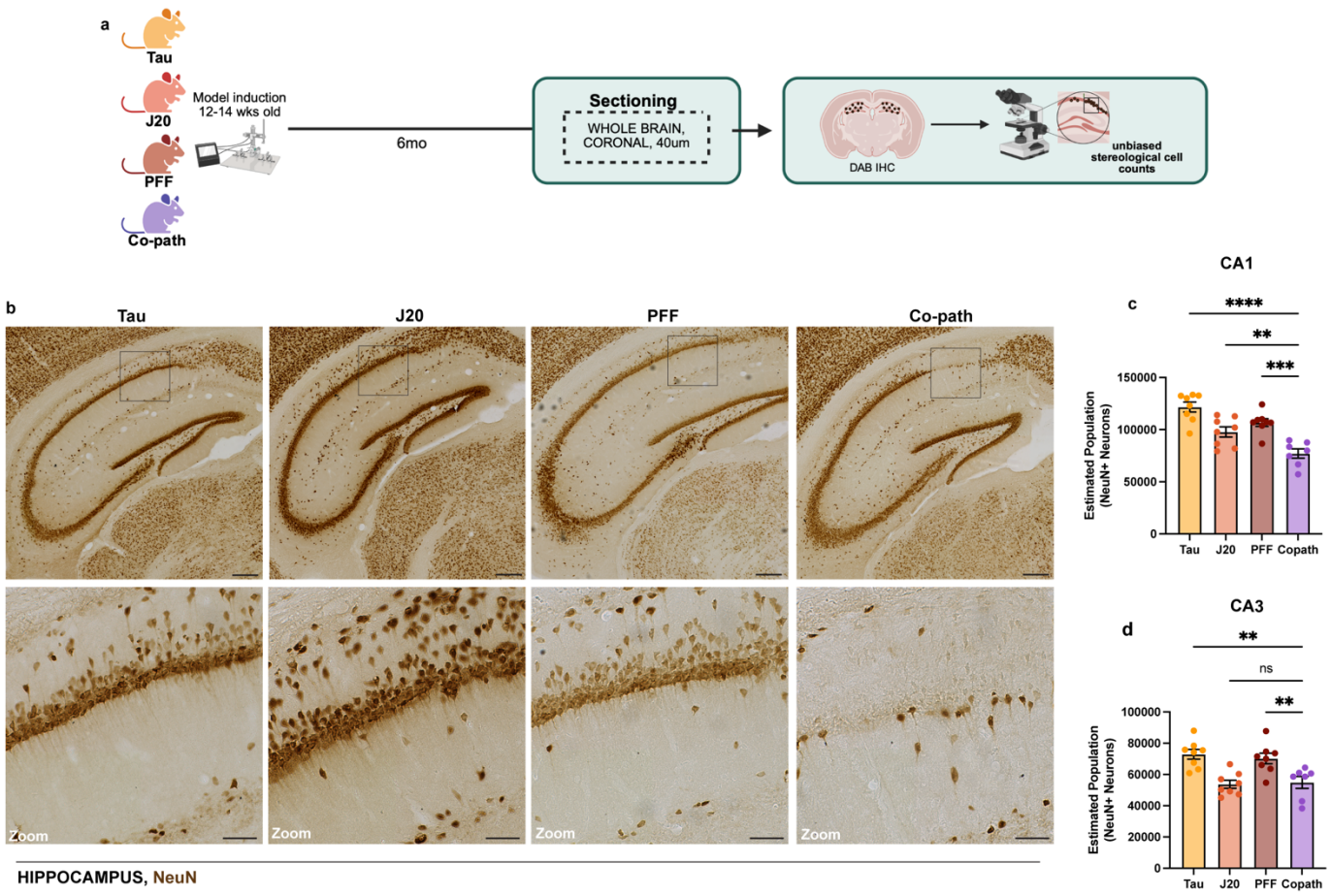

Figure 3. Co-pathologies drive enhanced neuronal loss in the hippocampus at 6MPI. (a) At 6MPI single pathology and co-pathology brains were processed for DAB IHC and unbiased stereology. (b) Representative brightfield images of NeuN+ neurons (DAB+, brown) in the hippocampus of Tau, J20 and PFF single pathology and co-pathology brain. Unbiased stereology was used to quantify the estimated number of NeuN+ neurons in the (c) CA1 and (d) CA3 regions of the hippocampus in the co-pathology mouse model compared to Tau, J20 and PFF single pathology brains. All images taken at 20X. Scale bars = 300µm and 100µm for zooms. One-way ANOVA with post hoc test was used to assess for significance. Mean values +/- SEM are plotted. ns = no significance, **p<0.01, ***p<0.005, ****p<0.0001. n=7-8 animals per group, both males and females used.

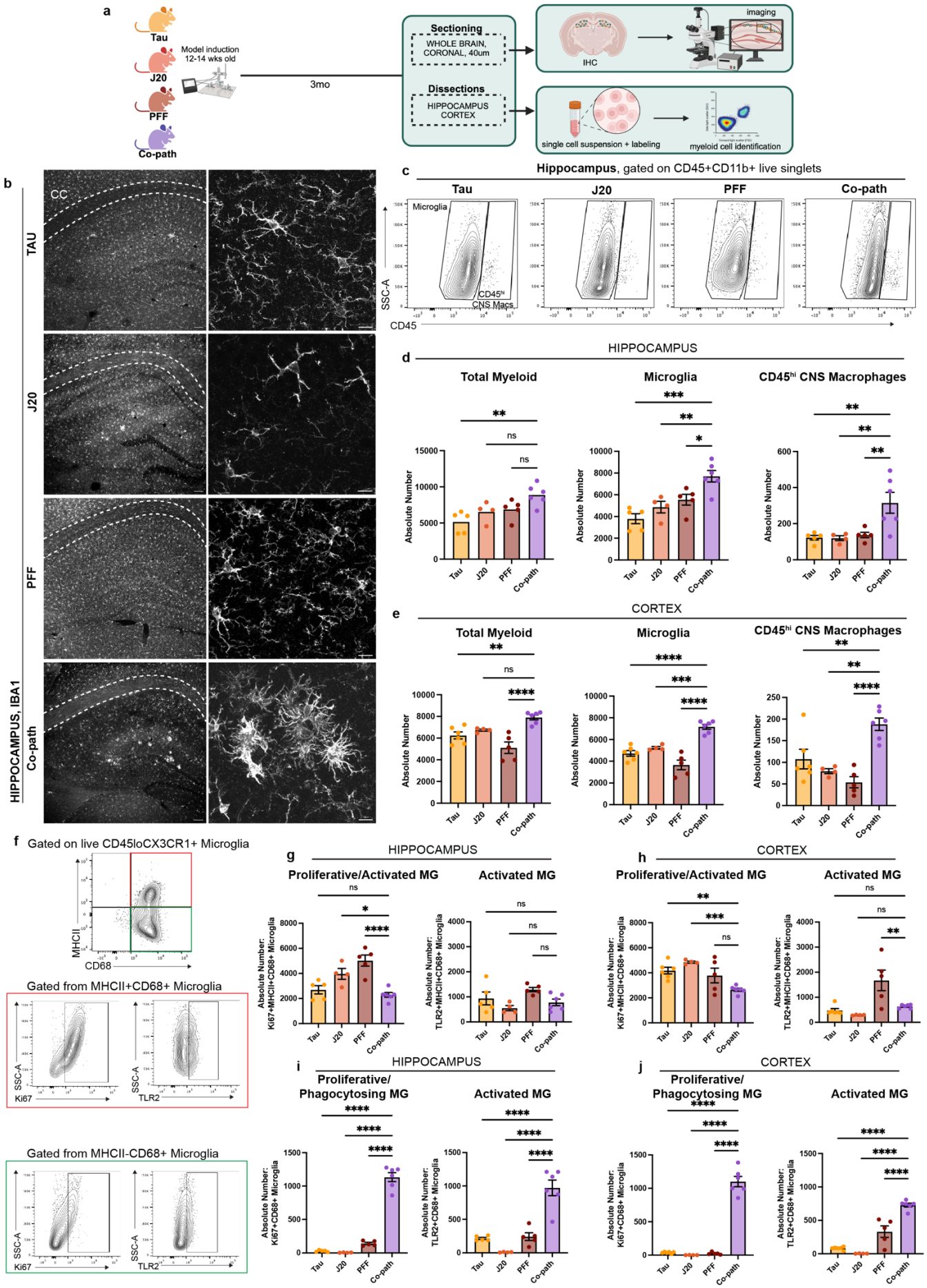
a
Tau
J20
PFF
Co-path
Model induction
12-14 wks old
3mo
Sectioning
WHOLE BRAIN, CORONAL, 40um
Dissections
HIPPOCAMPUS CORTEX
IHC
imaging
single cell suspension + labeling
myeloid cell identification
b
HIPPOCAMPUS, IBA1
TAU
J20
PFF
Co-path
CC
c
Hippocampus, gated on CD45+CD11b+ live singlets
Tau
J20
PFF
Co-path
Microglia
CD45hi CNS Macs
SSC-A
CD45
d
HIPPOCAMPUS
Total Myeloid
Microglia
CD45hi CNS Macrophages
Absolute Number
Tau
J20
PFF
Co-path
e
CORTEX
Total Myeloid
Microglia
CD45hi CNS Macrophages
f
Gated on live CD45loCX3CR1+ Microglia
MHCII
CD68
Gated from MHCII+CD68+ Microglia
SSC-A
Ki67
TLR2
Gated from MHCII-CD68+ Microglia
g
HIPPOCAMPUS
Proliferative/Activated MG
Activated MG
Absolute Number: Ki67+MHCII+CD68+ Microglia
Absolute Number: TLR2+MHCII+CD68+ Microglia
h
CORTEX
Proliferative/Activated MG
Activated MG
i
HIPPOCAMPUS
Proliferative/ Phagocytosing MG
Activated MG
Absolute Number: Ki67+CD68+ Microglia
Absolute Number: TLR2+CD68+ Microglia
j
CORTEX
Proliferative/ Phagocytosing MG
Activated MG

910 **Figure 4. Co-pathologies enhance microglia activation at 3MPI.** (a) J20 transgenic mice are
911 injected at 12-14 weeks of age with 2uL of 5ug α-syn PFFs and 2uL of 3.2E12 vg/mL AAV9-Tau
912 into the striatum and entorhinal cortex, respectively. For single pathology controls, age-matched
913 non-transgenic littermates are injected with α-syn PFFs into the dorsal lateral striatum for PFF
914 single pathology control or AAV9- Tau into the entorhinal cortex for Tau single pathology control.
915 Age-matched J20 mice are used as the Aβ single pathology controls. At 3MPI, brains were
916 collected and used for IHC or the hippocampus and surrounding cortices dissected and processed
917 for spectral flow cytometry. (b) Representative fluorescent grayscale images of Iba1+ microglia in
918 the hippocampus of Tau, J20 and PFF single pathology controls compared to that in the co-
919 pathology model. (c) Representative flow cytometry contour plots showing $CD45^{mid}$ microglia and
920 $CD45^{hi}$ CNS macrophages in single pathology and co-pathology hippocampus. The absolute
921 number of total myeloid cells, microglia and $CD45^{hi}$ infiltrating monocytes and resident
922 macrophages in the (d) hippocampus and (e) cortex of Tau, J20 and PFF only compared to co-
923 pathology brains are plotted. (f) From the $CD45^{mid}$ microglia population, representative contour
924 plots show expression of activation markers MHCII (antigen presentation, activated), CD68
925 (phagocytosing). The absolute number of $MHCII^{+}CD68^{+}$ microglia that are $Ki67^{+}$ or $TLR2^{+}$ in the
926 (g) hippocampus and (h) cortex of co-pathology and single pathology mice are plotted. $MHCII^{-}$
927 $CD68^{+}$ microglia that are $Ki67^{+}$ or $TLR2^{+}$ in the (i) hippocampus and (j) cortex of Tau, J20 and
928 PFF only compared to co-pathology brains are plotted. Analyzed using One-way ANOVA. Mean
929 values +/- SEM are plotted. *$p<0.05$, **$p<0.01$, ***$p<0.005$. n=5-6/group, with two brain regions
930 pooled per sampled, both males and females included in analysis. First panel images taken at 10X
931 magnification and zoomed, z-stack images at 40X. Scale bars (10X) = 100μm, scale bars (40X) =
932 10μm.

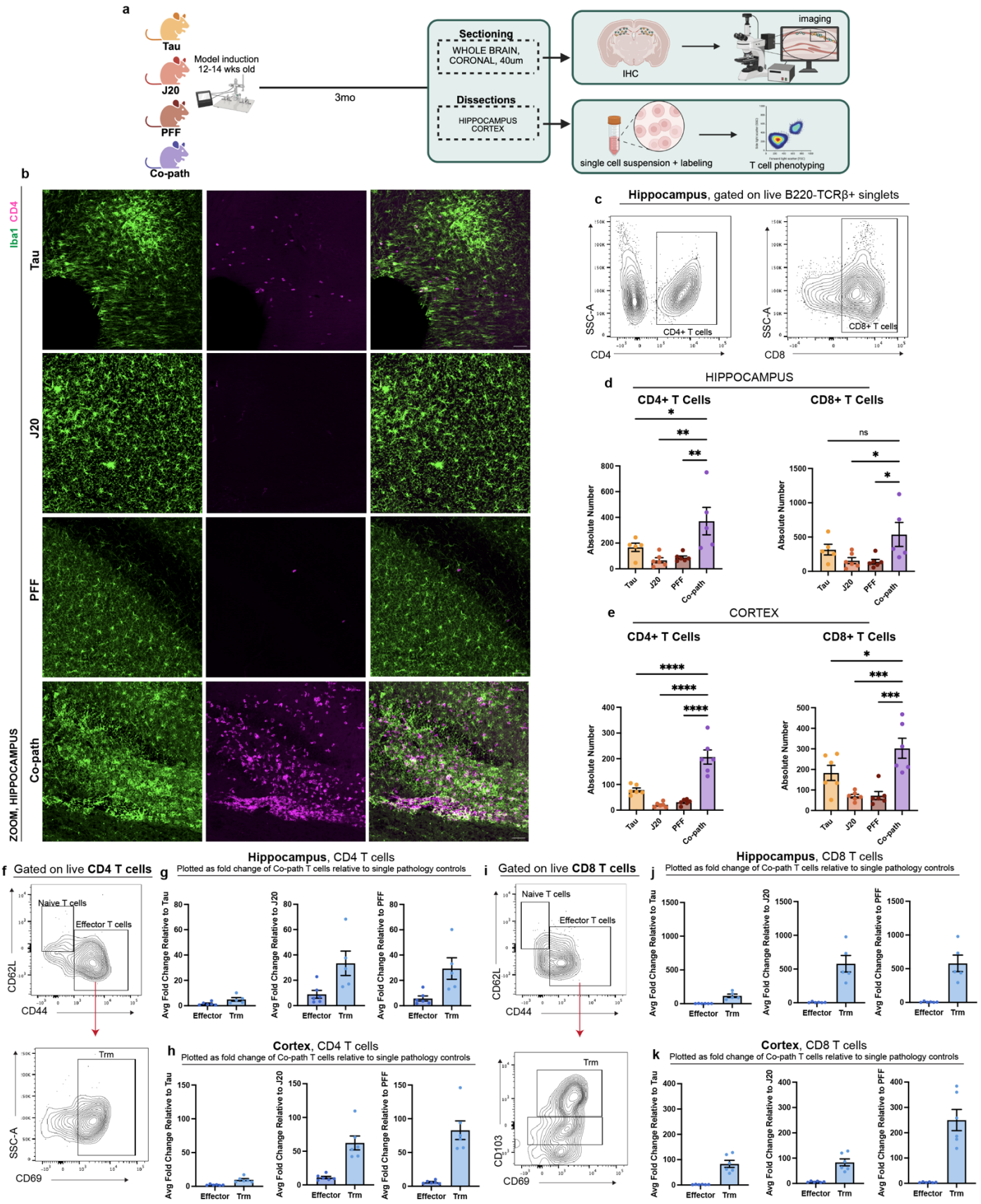
a
Tau
J20
PFF
Co-path
Model induction
12-14 wks old
3mo
Sectioning
WHOLE BRAIN, CORONAL, 40um
Dissections
HIPPOCAMPUS CORTEX
IHC
imaging
single cell suspension + labeling
T cell phenotyping
b
Iba1 CD4
Tau
J20
PFF
Co-path
ZOOM, HIPPOCAMPUS
c
Hippocampus, gated on live B220-TCRβ+ singlets
SSC-A
CD4+ T cells
CD4
CD8+ T cells
CD8
d
HIPPOCAMPUS
CD4+ T Cells
CD8+ T Cells
ns
Absolute Number
Tau
J20
PFF
Co-path
e
CORTEX
CD4+ T Cells
CD8+ T Cells
Absolute Number
Tau
J20
PFF
Co-path
f
Gated on live CD4 T cells
Naive T cells
Effector T cells
CD62L
CD44
Trm
SSC-A
CD69
g
Hippocampus, CD4 T cells
Plotted as fold change of Co-path T cells relative to single pathology controls
Avg Fold Change Relative to Tau
Avg Fold Change Relative to J20
Avg Fold Change Relative to PFF
Effector
Trm
h
Cortex, CD4 T cells
Plotted as fold change of Co-path T cells relative to single pathology controls
Avg Fold Change Relative to Tau
Avg Fold Change Relative to J20
Avg Fold Change Relative to PFF
Effector
Trm
i
Gated on live CD8 T cells
Naive T cells
Effector T cells
CD62L
CD44
Trm
CD103
CD69
j
Hippocampus, CD8 T cells
Plotted as fold change of Co-path T cells relative to single pathology controls
Avg Fold Change Relative to Tau
Avg Fold Change Relative to J20
Avg Fold Change Relative to PFF
Effector
Trm
k
Cortex, CD8 T cells
Plotted as fold change of Co-path T cells relative to single pathology controls
Avg Fold Change Relative to Tau
Avg Fold Change Relative to J20
Avg Fold Change Relative to PFF
Effector
Trm

933

934 **Figure 5. Co-pathologies promote T cell responses and tissue-resident memory T cell**
935 **phenotypes at 3MPI.** (a) J20 transgenic mice are injected at 12-14 weeks of age with 2uL of 5ug
936 α-syn PFFs and 2uL of 3.2E12 vg/mL AAV9-Tau into the striatum and entorhinal cortex,
937 respectively. For single pathology controls, age-matched non-transgenic littermates are injected
938 with α-syn PFFs into the dorsal lateral striatum for PFF single pathology control or AAV9- Tau
939 into the entorhinal cortex for Tau single pathology control. Age-matched J20 mice are used as the
940 Aβ single pathology controls. At 3MPI, brains were collected and the hippocampus and
941 surrounding cortices dissected and processed for spectral flow cytometry. (b) Representative
942 fluorescent images of Iba1+ microglia (green) and CD4+ T cells (magenta) in the hippocampus of
943 Tau, J20 and PFF single pathology controls compared to that in the co-pathology model. (c)
944 Representative flow cytometry contour plots show proportion for CD4+ and CD8+ T cells. The
945 absolute number of CD4+ and CD8+ T cells in the (d) hippocampus and (e) cortex of Tau, J20 and
946 PFF only compared to co-pathology brains are plotted. (f) Representative contour plot showing
947 expression and gating scheme of CD4+ Trm T cells. Quantified average fold change of CD44+
948 effector and CD69+ Trm in co-pathology (g) hippocampus and (h) cortex relative to Tau, J20 and
949 PFF single pathologies. (i) Representative contour plot showing expression and gating scheme of
950 CD8+ Trm T cells. Quantified average fold change of CD44+ effector and CD69+CD103+ Trm
951 in co-pathology (j) hippocampus and (k) cortex relative to Tau, J20 and PFF single pathologies.
952 Analyzed using One-way ANOVA. Mean values +/- SEM are plotted. *$p<0.05$, **$p<0.01$,
953 ***$p<0.005$. n=6/group, with two brain regions pooled per sampled, both males and females
954 included in analysis. All images taken at 10X magnification with z-stack, and digitally zoomed
955 using Nikon Elements software. Scale bars = 50μm.

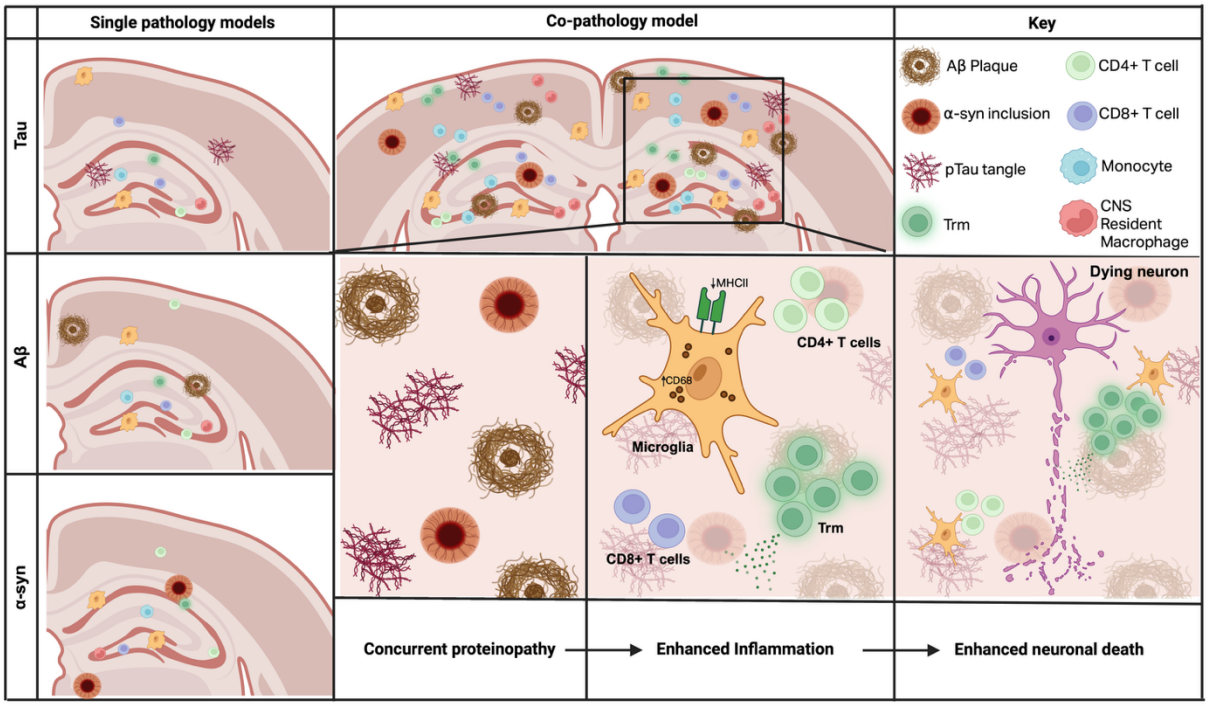

Figure 6. Synergistic effects of co-pathologies promote neuroinflammation, protein pathology load and neurodegeneration. Single pathology models (left panel) showing relatively mild immune activation and pathology, with little to no inclusion of tissue-resident memory (Trm) T cells, CD4+ and CD8+ T cells, monocytes and CNS resident macrophages. With the co-pathology model (middle panels), we demonstrate that concurrent protein aggregation, Aβ plaques, p-tau tangles and α-syn inclusions synergistically lead to increased recruitment and expansion of CNS-infiltrating immune cells including T cells and expanded Trm populations. This is accompanied by microglial morphology changes and elevated CD68+ expression and decreased number of MHCII+ cells. The cumulative effects of aggregated protein burden and chronic neuroinflammation result in neuronal damage and subsequent death.

970 # Methods

971 **Mice**

972 The mouse strain used for this research project, B6J.Cg-*Zbtb20*$^{Tg(PDGFB\text{-}APPSwInd)20Lms}$/Mmjax,
973 (RRID:MMRRC_034836-JAX), was obtained from the Mutant Mouse Resource and Research
974 Center (MMRRC) at The Jackson Laboratory, an NIH-funded strain repository, and was donated
975 to the MMRRC by Lennart Mucke, Ph.D., Gladstone Institute of Neurological Disease. Age and
976 sex-matched non-transgenic littermates (NTG, C57BL/6J background) were used for Sham and
977 single pathology induction. For all experiments presented, both male and female mice were used.
978 All research conducted on animals was approved by the Institutional Animal Care and Use
979 Committee at the University of Alabama at Birmingham and methods followed the Animal
980 Research: Reporting of *In vivo* Experiments (ARRIVE) 2.0 guidelines (arriveguidelines.org).

981

982 **Fibril and viral vector generation**

983 *Mouse α-synuclein pre-formed fibrils*

984 α-syn mouse pre formed fibrils (PFFs) were generated and purified from mouse α-synuclein from
985 the Volpicelli-Daley lab at the University of Alabama at Birmingham according to previously
986 published protocols (Luk et al., 2009, Volpicelli-Daley et al., 2014). Briefly, mouse PFFs were
987 thawed and aliquoted into 25uL (5mg/mL) and transferred to polystyrene sonication tubes. Tubes
988 containing PFFs were then transferred to a Q700 Sonicator water reservoir once the water was at
989 10C. Fibrils were sonicated for 15 minutes, with pulse on and off durations, at a power of
990 approximately 110 watts per pulse. After sonication, tubes are quickly spun down and 1uL of
991 sonicated PFFs transferred into an Eppendorf tube in 1X PBS, for a final volume of 500uL. 5uL

992 of this solution is sent for dynamic light scattering analysis to check for PFF fragmentation of
993 around 50nm after sonication.
994
995 *AAV9-Tau virus*
996 AAV double mutant (dbl^{mut}) tau (AAV9-Tau) genome plasmid was engineered by standard cloning
997 techniques to express human tau (2N4R isoform) encoding P301L/S320F mutations driven by the
998 hybrid chicken β-actin promoter and flanked by AAV2 iTRs.(Gray et al., 2011). Recombinant
999 adeno-associated virus capsid 9 (AAV9) vectors were generated as described in prior
1000 studies(Sandoval et al., 2019). Briefly, HEK293 cells were co-transfected with either dbl^{mut} tau or
1001 green fluorescent protein (GFP) genome plasmids, together with plasmids encoding AAV rep/cap
1002 genes and adenovirus helper proteins. AAV viral capsids were purified from cells and culture
1003 media by iodixanol gradient centrifugation, followed by dialysis in Dulbecco's PBS containing
1004 calcium and magnesium. Titers were determined by ddPCR using primers for the AAV iTRs and
1005 normalized to 3.2 viral genomes per mL (vg/mL).
1006
1007 **Stereotaxic injections**
1008 Mice aged 12-14 weeks old were deeply anesthetized using an isoflurane vaporizing instrument
1009 (UAB Animal Resource Program) and immobilized to a stereotaxic frame (Stoelting) on top of a
1010 heating pad to ensure appropriate internal body temperature is maintained. 26s/2"/2 10µL
1011 Hamilton syringes along with an automatic injecting system (Stoelting) are used to unilaterally
1012 (immunohistochemistry, DAB and fluorescence) or bilaterally (behavior, flow cytometry) inject
1013 2uL of mouse α-syn PFFs (5µg/mL), mouse α-syn monomer (5µg/mL), AAV9-dbl^{mut} tau virus
1014 (3.2E12vg/mL) or AAV9-GFP (3.2E12vg/mL). PFFs or monomer control were injected into the

1015 dorsal lateral striatum based on bregma (AP +0.5mm, ML +/-2.0mm and DV -3.0mm from the
1016 dura) AAV9-Tau or AAV9-eGFP viruses were injected into the entorhinal cortex (AP -3.5mm,
1017 ML +/-3.9mm and DV -4.2mm from dura). Injection needle was left in the injection site for an
1018 additional 2 minutes following completion and then slowly retracted from the site over the course
1019 of another 2 minutes. All surgical protocols and post-surgery aftercare methods were followed and
1020 approved by the Institutional Animal Care and Use Committee at the University of Alabama at
1021 Birmingham.
1022 To induce the co-pathology model, 3-month-old J20 transgenic mice were injected with mouse α-
1023 syn PFFs into the striatum and AAV9-Tau virus into the entorhinal cortex. For sham surgery, non-
1024 transgenic (NTG) littermates were injected with mouse α-syn monomer and AAV9-eGFP into the
1025 striatum and entorhinal cortex, respectively.
1026 To induce single pathology controls, NTG mice were injected with mouse α-syn PFFs into the
1027 dorsal lateral striatum for α-syn models and AAV9-Tau virus into the entorhinal cortex for tau
1028 models. α-syn monomer into the striatum and AAV9-GFP were injected into the dorsal lateral
1029 striatum and entorhinal cortex, respectively, of non-transgenic mice as controls. J20 transgenic
1030 mice were used as the Aβ single pathology mice, compared to un-injected NTG littermates.
1031

1032 **Tissue preparation and processing**

1033 At 3 months post-induction (3MPI) and 6 months post-induction (6MPI) of the co-pathology
1034 model and single-color controls, mice were anesthetized using isoflurane and transcardially
1035 perfused with 0.01M phosphate-buffered saline (PBS, pH = 7.4) and fixed with 4%
1036 paraformaldehyde (PFA in PBS, pH = 7.4). Brains were then dissected and incubated in 4% PFA
1037 for 2 hours at room temperature. After fixation, brains were placed in 30% sucrose in PBS for 3

1038 days until brains were fully saturated. Brains were then frozen on dry ice and cryosectioned
1039 coronally at 40µm on a sliding microtome (Thermo Scientific Micron HM 450). Sliced brain tissue
1040 was then stored in a 50% glycerol/PBS solution at -20ºC.
1041
1042 **Immunofluorescent immunohistochemistry**
1043 Free-floating 40-µm thick sections were washed in 0.01M tris-buffered saline solution (TBS, pH
1044 7.4) prior to an antigen retrieval process with a solution of 10mM sodium citrate and 0.05% Tween-
1045 20 in TBS. Sections were then incubated in 5% blocking serum at room temperature before being
1046 incubated overnight in the following primary antibody solutions (TBST, 1% serum): anti-CD4
1047 (clone RM4-5, ThermoFisher), anti-CD8 (clone 4SM15, eBioscience) and anti-Iba1 (WACO). On
1048 the following day, sections were washed in TBS with .1% Triton-100 and incubated in fluorescent
1049 conjugated antibody in the dark for 2 hours at room temperature. Sections were then washed in
1050 TBST and mounted on microscope slides for analysis. Slides were imaged at 20X on a Nikon A1
1051 Laser Scanning Confocal microscope.
1052
1053 **DAB immunohistochemistry**
1054 Free-floating 40-µm thick sections were washed in 0.01M tris-buffered saline solution (TBS, pH
1055 7.4) prior to being quenched with 3% hydrogen peroxide in TBS for 5 minutes. Next, sections
1056 underwent an antigen retrieval process with a solution of 10mM sodium citrate and 0.05% Tween-
1057 20 in TBS for 30 minutes at 37ºC. Following this, sections were blocked in a 5% goat or donkey
1058 serum solution for at least 1 hour at room temperature and then incubated overnight at 4ºC with
1059 the following antibodies in 1% serum solution: anti-CD3 (clone 17A2, eBioscience), anti-tyrosine
1060 hydroxylase (clone: EP1536Y, Abcam), anti-alpha synuclein, phosphor-serine 129 (pSer129, close

1061 EP1536Y, Abcam), anti-AT8 (clone MN1020, ThermoFisher), anti-Aβ (clone D54D2, Cell
1062 Signaling) and anti-NeuN (clone EPR12763, Abcam). Sections were then incubated with a
1063 biotinylated secondary antibody (1:1000, Vector Labs) in a 1% serum in TBST solution. After
1064 incubation, sections were washed with TBS and incubated in the Vectastain ABC Reagent (Vector
1065 Labs) for 30 minutes at RT prior to development with the Vectastain diaminobenzidine DAB Kit
1066 (SK-4199, Vector Labs) according to the manufacturer's protocol. Sections were then mounted
1067 onto plus-coated slides and dehydrated with a gradient of ethanol solutions (70%-100%) followed
1068 by Citrisolv. Slides were them coverslipped with Permount Mounting Media (Electron Microscopy
1069 Sciences). Slides were then images at 10X and 20X on a Zeiss Imager M2 brightfield microscope
1070 (MBF Biosciences).
1071
1072 **Unbiased stereology of the hippocampus and substantia nigra pars compacta**
1073 In order to quantify neuronal cell loss, an unbiased stereology protocol was used. TH and NeuN-
1074 DAB stained (see 'DAB Immunohistochemistry' section) SNpc and hippocampal tissue sections,
1075 respectively, were imaged and analyzed with a Zeiss Axio Imager M2 microscope (MBF
1076 Biosciences) and the Cavalieri stereology probe used to count cells, with a section thickness of
1077 25µm to account for dehydration of sections. To quantify NeuN+ neurons in the hippocampus,
1078 contours were drawn around the five to seven sections, focusing on the CA1 and CA3 regions. To
1079 quantify Th+ neurons in the SNpc, contours were drawn around both sides of the nigra, in four to
1080 five sections. Similar contours were drawn in the nigra to quantify α-syn+ neurons. For
1081 stereological counting, the grid size used for the hippocampus was 130µmx130µm and the
1082 counting frame was 40µmx40µm. In the SNpc, the grid size and counting frame were, 100x100
1083 and 50µmx50µm, respectively.

1084

1085 **Brain single cell isolation and flow cytometry**

1086 At 3MPI, co-pathology and single pathology mice were anesthetized and transcardially perfused
1087 with 0.01M PBS (pH 7.4). Briefly, brain tissue was removed and the brain regions dissected.
1088 Tissue was then digested with 1 mg/mL Collagenase IV (Sigma) diluted in RPMI 1640 (1X,
1089 Gibco). Following enzyme digestion, tissue was then filtered and smashed through a 70μm filter
1090 using a syringe plunger and mononuclear cells isolated out using a 30/70% Percoll gradient (GE).

1091

1092 For cell staining, isolated brain cells were blocked with anti-Fcγ receptor (1:100, Biosciences).
1093 Following this, cell surface markers were labelled with the following, fluorescent-conjugated
1094 antibodies against CD45 (clone 30-F11, eBioscience), CD11b (clone M1/70, BioLegend), MHCII
1095 (M5/114.15.2, BioLegend), Ly6C (clone HK 1.4, BioLegend), TCRβ (clone H57-597, Biolegend),
1096 CD4 (GK1.5, BioLegend), CD8a (clone 53-6.7, BioLegend). CD69 (clone H1.2F3, BioLegend), ,
1097 B220 (clone RA3-6B2, BD Biosciences), CD44 (clone IM7, Biolegend), CD62L (clone MEL-14,
1098 BioLegend), CD103 (clone 2E7, BioLegend), TLR2 (clone CB225, BD Biosciences), Ki67 (clone
1099 16A8, BioLegend), CX3CR1 (clone SA011F11, BioLegend), CD68 (clone FA-11, BioLegend). A
1100 fixable viability dye was used to distinguish live cells, per the manufacturer's protocol Aqua-
1101 LIVE/DEAD Stain Kit (Invitrogen). As single-color compensation controls, isolated splenocytes
1102 or UltraComp eBeads™ (Invitrogen) were used. To analyze and run samples, a BD Symphony
1103 (BD Biosciences) or Spectral Enabled Symphony flow cytometer were used at the UAB Flow
1104 Cytometry and Single Cell Core Facility. Mean cell counts, percentages and mean fluorescent
1105 intensity were measured and analyzed using FlowJo (Tree Star) software.

1106

1107 **Mouse brain lysate preparation**

1108 Brain tissue was micro dissected, snap frozen in super-cooled bath of 2-methylbutane with dry ice,
1109 and stored at -80°C. Tissue lysates were homogenized with a tissue grinder using 20%
1110 weight/volume lysis buffer (50 mmol/L Tris-HCl pH 7.4, 175 mmol/L NaCl, 5 mmol/L EDTA)
1111 supplemented with protease and phosphatase inhibitors and sonicated for 10 sec on ice. After
1112 addition of Triton X-100 to a final concentration of 1% volume/volume, samples were incubated
1113 on ice for 30 minutes and centrifuged at 15,000 xg for 60 min at 4°C. The supernatant was saved
1114 as the Triton X-100 soluble fraction. The pellet was resuspended in lysis buffer with 2% SDS,
1115 sonicated for 10 sec, and centrifuged for 10 minutes at 15,000 xg. The resulting supernatant was
1116 reserved as the Triton X-100 insoluble fraction. Protein concentration was determined by the
1117 bicinchoninic acid assay (Pierce Cat# 23225).

1118

1119 **Amyloid β detection by Aβ1-42 ELISA**

1120 A total of 20 µg brain lysate was used to measure concentration of Aβ1-42 with the human
1121 Amyloid beta (aa1-42) Quantikine ELISA (R&D Systems Cat# DAB142) kit following the
1122 manufacturer's protocol. Colorimetric signal was measured using the SpectraMax iD3 (Molecular
1123 Devices).

1124

1125 **Western Blot**

1126 *Chemiluminescence*

1127 A total of 20µg of protein from the Triton X-100 soluble and insoluble fractions described above
1128 were denatured in dithiothreitol (DTT) buffer (0.25 M Tris-HCl pH 6.8, 200mM DTT, 8% SDS,
1129 30% glycerol, 2mg bromophenol blue) by boiling for 10m. Samples were run on 15% SDS-

1130 polyacrylamide gels and transferred onto nitrocellulose membranes, which were then fixed for
1131 30m in 0.4% paraformaldehyde. Blots were blocked in 5% dry milk in TBS-T for 1 hour at ambient
1132 temperatures and incubated in primary antibodies at 4ºC overnight. Primary antibody
1133 concentrations are as follows: Alpha-Synuclein (1:1000; BD-Biosciences 610787) and GAPDH
1134 (1:10,000; Cell Signaling 14C10). Blots were washed in TBS-T, incubated in HRP-conjugated
1135 secondary antibodies (Mouse HRP: Jackson Labs 115-035-003; Rabbit HRP: Jackson Labs 111-
1136 035-003) at 1:2000 for 1h at ambient temperatures, and imaged using a BioRad ChemiDoc MP
1137 system. Blots were analyzed using BioRad Image Lab software.

1138 *Fluorescence*

1139 Blots were run as described above. LI-COR blocking buffer and antibody diluents (LI-COR 927-
1140 66003) were used with Tau (1:1000; Cell Signaling 43984S) and GAPDH antibodies. IRDye-
1141 conjugated secondary antibodies (Mouse IRDye 680: LI-COR 926-68070; Rabbit IRDye 800: LI-
1142 COR 926-32211) were used at 1:2000 for 1h at ambient temperatures. Blots were imaged using a
1143 LI-COR Odyssey CLx system and analyzed using LI-COR Image studio software.

1144

1145 **Dendritic spine morphology analysis**

1146 *Perfusions and brain tissue processing*

1147 For iontophoretic microinjections, mice were anesthetized with Fatal Plus (Vortech
1148 Pharmaceuticals, Catalog #0298-9373-68) and transcardially perfused with cold 1%
1149 paraformaldehyde (PFA; Sigma Aldrich, Catalog #P6148) for 1 min, followed by 4% PFA with
1150 0.125% glutaraldehyde (Fisher Scientific, Catalog #BP2547) for 10 min. A peristaltic pump
1151 (Cole Parmer) was used for consistent administration of cold PFA. Immediately following
1152 perfusion, each brain was extracted and drop-fixed in 4% PFA with 0.125% glutaraldehyde for

8–12 h at 4 °C. After fixation, brains were coronally sliced in 250 µm thick sections using a Leica vibratome (VT1000S, speed 70, frequency 7). Brains were sliced in 0.1 M PB and stored at 4 °C, one slice per well in a 48-well plate, in 0.1 M PB with 0.1% sodium azide (Fisher, Catalog #BP922I).

Iontophoretic microinjections

Iontophoretic microinjections were performed based on methods described previously(Greathouse et al., 2019, Henderson et al., 2019). A Nikon Eclipse FN1 upright microscope with a 10× objective and a 40× water objective was placed on an air table. The tissue chamber used consisted of a 50 × 75 mm plastic base with a 60 × 10 mm petri dish epoxied to the base. A platinum wire was attached so that the ground wire could be connected to the bath by an alligator clip. The negative terminal of the electric current source was connected to a glass micropipette filled with 2 µL of 8% Lucifer yellow dye (ThermoFisher, Catalog#L453). Micropipettes (A-M Systems, Catalog #603500) with highly tapered tips were pulled fresh at the time of use. A manual micromanipulator was secured on the air table with magnets that provided a 45° angle for injection. Brain slices were placed into a small petri dish containing 1× PBS and DAPI for 5 min at room temperature. After incubation in DAPI, slices were placed on dental wax, and then a piece of filter paper was used to adhere the tissue. The filter paper was then transferred to the tissue chamber filled with 1× PBS, and weighted down for stability. The 10× objective was used to visualize advancement of the tip of the micropipette in X, Y, and Z planes until the tip was just a few micrometers above the tissue. The 40× objective was then used while advancing the tip into layer 2/3 of the ventral CA1 regions of the hippocampus. Once the microelectrode contacted a neuron, 2 nA of negative current were applied for 5 min to fill the

1176 neuron with Lucifer yellow. After 5 min, the current was turned off and the micropipette was
1177 removed from the neuron. Neuron impalement within the CA1 occurred randomly in a blind
1178 manner. If the entire neuron did not fill with dye after penetration, the electrode was removed
1179 and the neuron was not used for analysis. Multiple neurons were injected in each hemisphere of
1180 each animal. After injection, the filter paper containing the tissue was moved back into the
1181 chamber containing 1× PBS. The tissue was carefully lifted off the paper and placed on a glass
1182 slide with two 125 µm spacers (Electron Microscopy Sciences, Catalog #70327-20S). Excess
1183 PBS was carefully removed with a Kimwipe, and the tissue was air-dried for 1 min. One drop of
1184 Vectashield (Vector Labs, Catalog #H1000) was added directly to the slice, and the coverslip
1185 (Warner, Catalog #64-0716) was added and sealed with nail polish. Injected tissue was stored at
1186 4 °C in the dark.
1187
1188 *Confocal microscopy*
1189 Confocal microscopy was used to capture images of Lucifer yellow-filled dendrites on pyramidal
1190 neurons in CA1 of the hippocampus. Our methods are based on previously described
1191 methods(Greathouse et al., 2018, Henderson et al., 2019), and are detailed as follows. Imaging
1192 was performed by a blinded experimenter on a Nikon (Tokyo, Japan) Ti2 C2 confocal
1193 microscope, using a Plan Apo 60×/1.40 NA oil-immersion objective. Three-dimensional z-stacks
1194 were obtained of secondary dendrites from dye-impregnated neurons that met the following
1195 criteria: (1) within 80 µm working distance of microscope, (2) relatively parallel with the surface
1196 of the coronal section, (3) no overlap with other branches, (4) located between 40 and 120 µm
1197 from the soma. Nikon Elements 4.20.02 image capture software was used to acquire z-stacks

1198 with a step size of 0.1 μm, image size of 1024 × 512 px, zoom of 4.8×, line averaging of 4×, and
1199 acquisition rate of 1 frame/s.
1200 Confocal microscopy was also used to capture images of slices from mice. Imaging was
1201 performed on a Nikon Ti2 C2 confocal microscope, using a Plan Fluor 10×/0.75 NA air
1202 objective. Nikon Elements 4.20.02 image capture software was used to acquire stitched images
1203 (20 × 10 field) by automatically stitching multiple adjacent 10× images using 25% blending
1204 overlap. Each frame had an image size of 1024 × 1024 px, and acquisition rate of 1 frame/s.
1205 Subsequently, 10× stitched images were acquired, with all other imaging parameters remaining
1206 the same. Following image acquisition, post-image processing was performed using Fiji ImageJ.
1207 Each image file was a two channel image. The Split Channels function was used to separate the
1208 two channels.
1209
1210 *Dendritic spine morphometry analysis*
1211 Confocal z-stacks of dendrites were deconvolved using Huygens Deconvolution System (16.05,
1212 Scientific Volume Imaging, the Netherlands). The following settings were used: deconvolution
1213 algorithm: GMLE; maximum iterations: 10; signal to noise ratio: 15; quality: 0.003.
1214 Deconvolved images were saved in .tif format. Deconvolved image stacks were imported into
1215 Neurolucida 360 (2.70.1, MBF Biosciences, Williston, Vermont) for dendritic spine analysis. For
1216 each image, the semi-automatic directional kernel algorithm was used to trace the dendrite. The
1217 outer 5 μm of each dendrite were excluded from the trace. All assigned points were examined to
1218 ensure they matched the dendrite diameter and position in X, Y, and Z planes, and were adjusted
1219 if necessary. Dendritic spine reconstruction was performed automatically using a voxel-
1220 clustering algorithm, with the following parameters: outer range = 5 μm, minimum

1221 height = 0.3 μm, detector sensitivity = 80%, minimum count = 8 voxels. The semi-automatically
1222 identified spines were examined to ensure that all identified spines were real, and that all existing
1223 spines had been identified. If necessary, spines were added by increasing the detector sensitivity.
1224 Additionally, merge and slice tools were used to correct errors made in the morphology and
1225 backbone points of each spine. Each dendritic spine was automatically classified as a dendritic
1226 filopodium, thin spine, stubby spine, or mushroom spine based on constant
1227 parameters(Greathouse et al., 2019, Henderson et al., 2019). Three-dimensional dendrite
1228 reconstructions were exported to Neurolucida Explorer (2.70.1, MBF Biosciences, Williston,
1229 Vermont) for branched structure analysis, which provides measurements of dendrite length;
1230 number of spines; spine length; number of thin, stubby, and mushroom spines, and filopodia;
1231 spine head diameter; and spine neck diameter, among other measurements. The output was
1232 exported to Microsoft Excel (Redmond, WA). Spine density was calculated as the number of
1233 spines per 10 μm of dendrite length. Values per mouse were calculated by averaging the values
1234 for all dendrites corresponding to that mouse. To assess apical and basal dendrites separately,
1235 values for either apical or basal dendrites were averaged per mouse. For a mouse to be included
1236 in statistical analyses for dendritic spine density and morphology a minimum of 100 μm of
1237 dendrite length had to be reconstructed and analyzed.
1238
1239 **Behavior**
1240 Behavior tests to assess for motor and cognitive function were conducted at 6 months post-
1241 induction of co-pathology model or single pathology models. Mice were handled for 3 days prior
1242 to the start of testing and were habituated to the testing room for 1 hour at the start of each testing
1243 day. The order of test was designed to minimize stress to the animals, such that lower-stress tasks

1244 were completed before high-stress tasks. All apparatus was cleaned with 2% chlorohexadine
1245 between trials. The researcher conducting the tests was blinded to experimental groups during
1246 trials and analysis.

1247 *Open Field*

1248 To test for general motor activity, mice were place in a 30.48 x 30.48 cm enclosed field with
1249 opaque walls and allowed to explore for 10 minutes. The inner zone was defined as the center of
1250 the box. Noldus Average velocity, distance traveled, and percent of the time spent in the center
1251 were determined by the Ethovision XT v16 software.

1252 *Pole Test*

1253 To further test for motor deficits, mice were placed in a dark room and habituated for 1 hour
1254 starting at the beginning of the dark phase. Two red lamps were strategically placed in the room
1255 to visualize the behavior test without disrupting the dark phase. The pole test was performed
1256 using a 53cm wooden dowel rod with a diameter of 10 mm, anchored with a 13.9 x 20 x 1.8 cm
1257 block of wood and ridged at 2.54 cm intervals with rolled rubber bands. The dowel rod was
1258 placed vertically in the center of a 1x1 foot enclosure. The mice were first trained by being
1259 placed face-down at the base of the pole and allowed to climb off onto the floor of the enclosure
1260 before being returned to their cage. This training was done twice. Following this, each mouse
1261 was placed face-up at the top of the pole and allowed no more than 180 seconds to turn around
1262 and climb down to the bottom; this was repeated five times. Mice were given a minimum of 30
1263 seconds to rest between each trial. Three time point measurements were recorded. The first time
1264 point started from the time the mouse was placed on the pole to the time taken for the mouse to
1265 reach the bottom (total descent time). Measurements were recorded for the time the mouse took
1266 to turn around on the pole to face the bottom (turnaround time) and the total time to descend

(time descending) in seconds. The average time for each time point was calculated from all five trials for each mouse.

Rotarod

To further test for motor activity, mice were placed on an accelerating rotarod apparatus, and time taken to fall was measured. Mice were trained on the apparatus over 5 days, with the rotarod speed increasing from 4 rpm to 40 rpm over 300 seconds. If mice had not fallen by 120 seconds during the testing trial, the rotation was paused, mouse was removed, and the time was recorded as 120 seconds. Mice underwent two trials per day with 30 minutes of resting time between each trial.

Barnes Maze

A blue circular apparatus of 122cm in diameter consisting of forty, five cm, evenly spaced holes was used throughout the test. The test consisted of three stages: (1) Habituation phase, (2) Acquisition phase, and (3) Probe phase. The habituation phase took place on day 1 where mice were placed in the center of the apparatus covered by a black mesh cup uniformly covered. 10 seconds after the placement, mice freely roamed the Barnes maze for an undefined amount of time until they found and independently entered the escape tunnel. The acquisition phase occurred through Days 2-6 and consisted of one, five-minute trial. If mice did not find nor enter the escape tunnel after the five-minute trial, mice were gently guided towards the direction of the tunnel where they then entered it on their own. Entry into the tunnel was defined as all four paws in the tunnel. Upon entry, a cover was used to cover to hole to prevent the mice from leaving the tunnel. The tunnel was then carefully removed from the maze apparatus and gently placed in the home cage of the mouse. The latency to find and enter the escape tunnel was recorded. On Day 10, mice were again introduced to the maze for one minute without the escape tunnel present.

1290 The amount of time spent in the escape tunnel quadrant, entry zone, and goal box were
1291 determined by the Ethovision XT v16 software.
1292
1293 **Statistical Analysis**
1294 All graphs and subsequent statistical tests were generated using Prism software (GraphPad). Flow
1295 cytometry experiments used ten to twelve independent samples with two brain regions pooled per
1296 sample, for a final number of five to six per group for experiments. Data were analyzed using an
1297 unpaired student's t-test or a one-way ANOVA. Graphs within display the mean +/- SEM. For
1298 unbiased stereology, estimated populations were generated and a one-way ANOVA was used to
1299 determine the significance between groups. *$p<0.05$, **$p<0.01$, ***$p<0.0005$, ****$p<0.0001$.
1300
1301 **Data availability**
1302 The authors affirm that the findings within the manuscript are supported by the data therein. The
1303 data, protocols and key lab materials used and generated in this study are listed in a Key Resource
1304 Table alongside their persistent identifiers on Zenodo (10.5281/zenodo.16739907).
1305

1306 Declarations

1307 **Acknowledgements**
1308 We would like to thank Josh Randolph for maintenance and assistance with animal husbandry and
1309 handling. We thank Rajesh Gupta for his preliminary contributions to immunohistochemistry
1310 staining. We thank Veronica Obregon-Perko for her assistance with spectral flow cytometry panel
1311 design. We also thank Laura Volpicelli-Daly, Charlotte Brzozowski and Marissa Menard for their
1312 contribution of mouse α-syn PFFs for our studies. Lastly, we would like to thank Warren Hirst,

Lucas Hampton and Karen Eskow-Jaunarajs for their input and guidance during the development of this project. We thank the UAB Comprehensive Flow Cytometry Core for their assistance with flow cytometry experiments. The core is supported by the Center for AIDS Research, AI027767, The O'Neal Comprehensive Cancer Center, CA013148 and Shared instrument grant S10OD032296. Experimental design figures were generated using BioRender. This work was supported in whole by Aligning Science Across Parkinson's (Grant# ASUB00000984) through the Michael J. Fox Foundation for Parkinson's Research (MJFF). For the purposes of open access, the author has applied a CC BY public copyright license to all Author Accepted Manuscripts arising from this submission.

Author's contributions

JMW and ASH designed the study, experiments, and wrote the manuscript. JMW was responsible for planning and performing all stereotaxic surgeries. JMW, YTY, ATM, NJCS, WJW and AZ contributed towards tissue collection and executing flow cytometry experiments. TAY, WJS, KS and JMW performed all ELISA and immunoblotting experiments and analysis. JMW, NM and ACS conducted IHC stains. JMW manually assessed NeuN+ neuronal loss via unbiased stereology. AZ manually assessed Th+ neuronal loss via stereology. NHC, LFL, PNM, KMG and JHH planned, conducted and analyzed dendritic spine morphology counts. FPM and IS developed and optimized the AAV double-mutant tau vector. JMW and ASH drafted and constructed the manuscript and figures. FPM, JHK and DJT provided feedback on study design and edits to the manuscript. All authors read and approved the final manuscript.

Competing interests

The authors have no competing interests.

Supplemental Figures

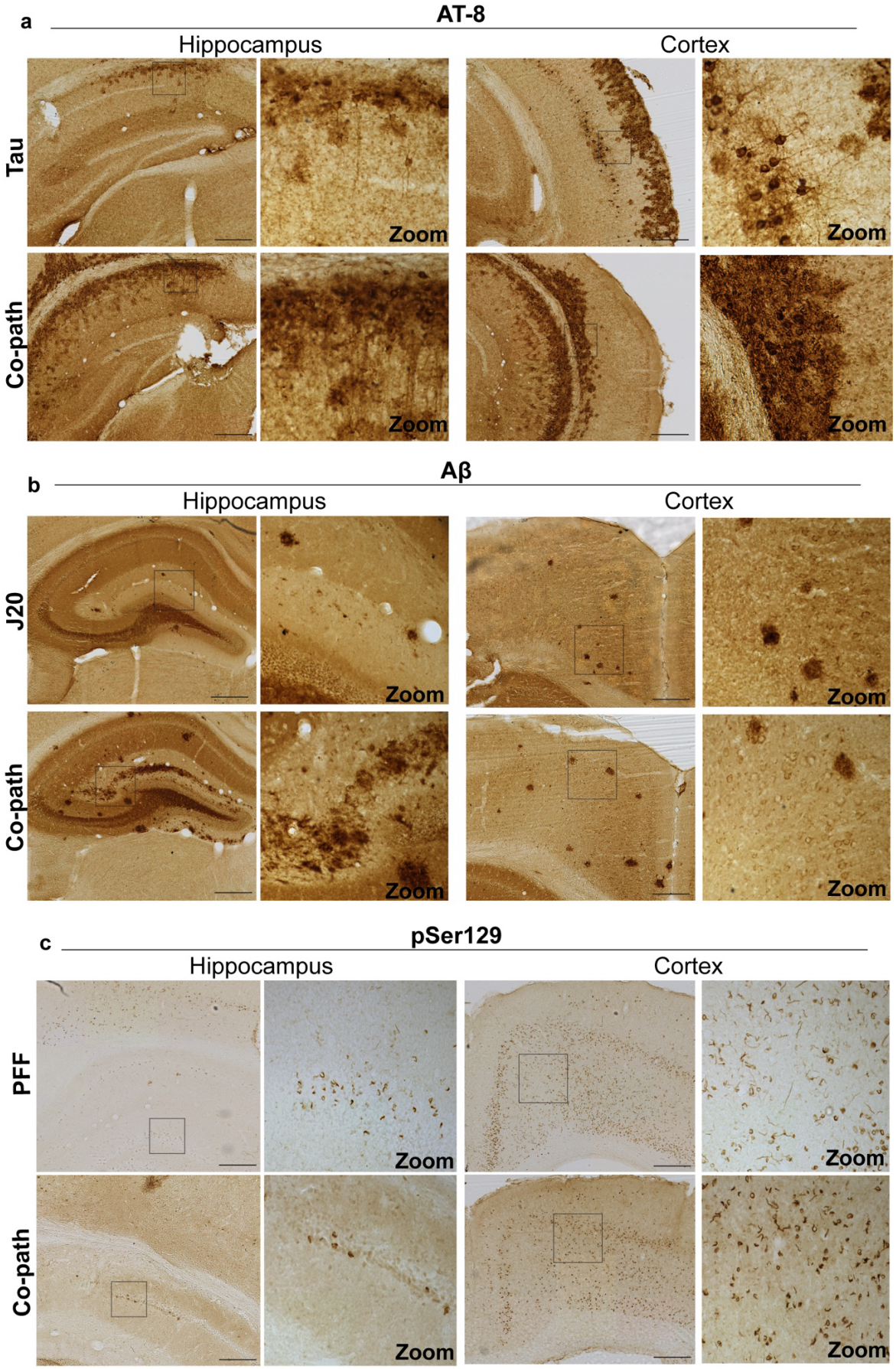
a
AT-8
Hippocampus
Cortex
Tau
Co-path
Zoom
b
Aβ
Hippocampus
Cortex
J20
Co-path
Zoom
c
pSer129
Hippocampus
Cortex
PFF
Co-path
Zoom

1339

1340 **Supplemental Figure 1. AT-8, Aβ or pSer129 protein pathology at 6MPI in the hippocampus**
1341 **and cortex of co-pathology and single pathology brains.** (a) AT-8/pTau-positive neurons
1342 (DAB+, brown) in the hippocampus and cortex of tau single pathology and co-pathology brains.
1343 (b) Aβ-positive plaques (DAB+, brown) expressed in the hippocampus and cortex of J20 single
1344 pathology and co-pathology brains. (c) pSer120-positive inclusions in the hippocampus and cortex
1345 of PFF only (α-syn) and co-pathology brains. All images taken at 10X or 20X for zooms, scale
1346 bars = 100μm.
1347
1348
1349

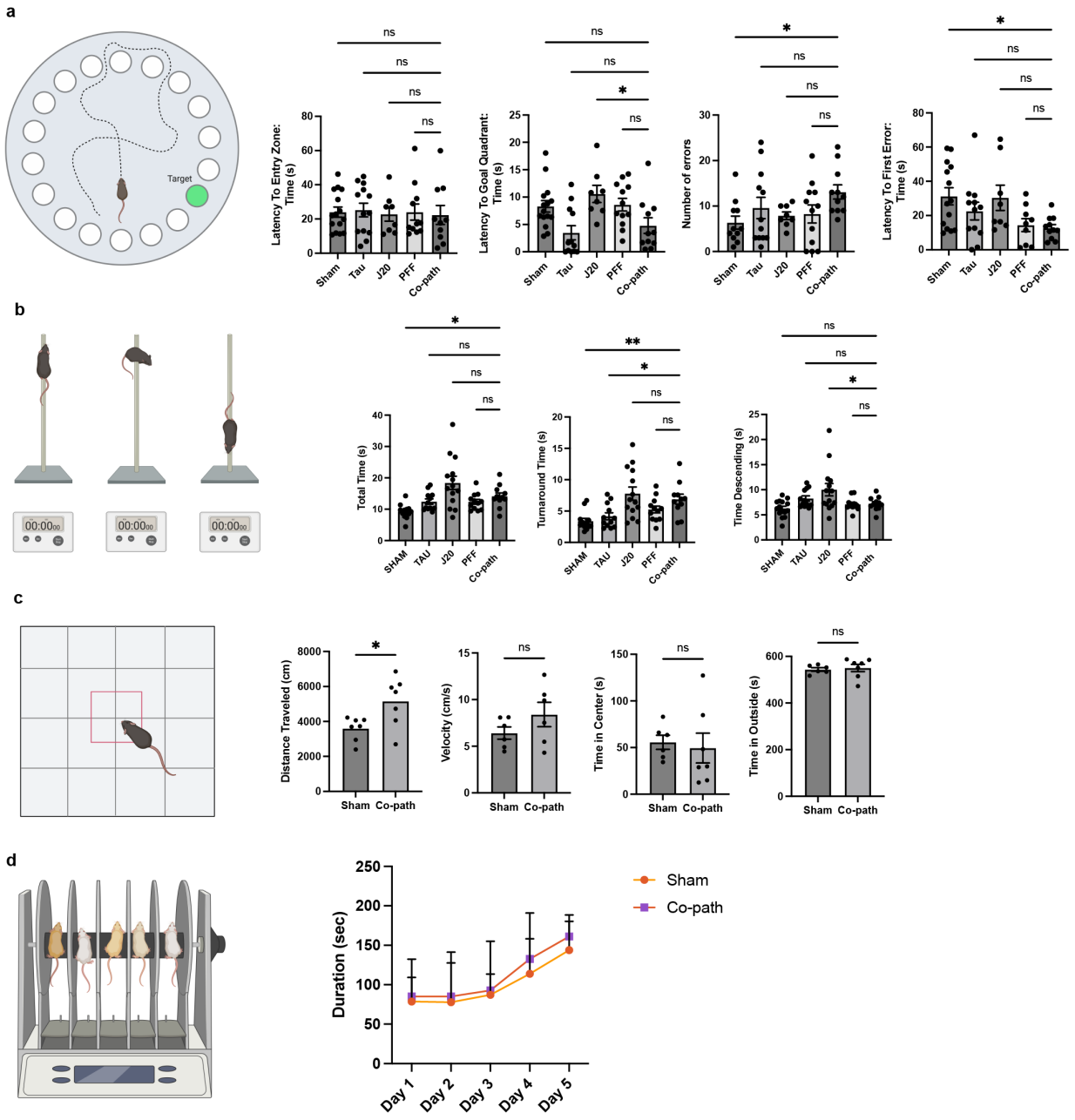

Supplemental Figure 2. Motor and cognitive behavioral tests to assess for impairments in co-pathology vs single pathology animals. (a) Quantification of latency to entry zone, to goal quadrant, to first error and the total number of errors analyzed from Barnes maze test. (b) Measures of total time, turnaround time and time descending on the pole test. (c) Distance travelled, velocity, time in center and time in outside are depicted from open field test. (d) Total duration of animals on rotarod platform across 5 days of testing. Student's t-test or One-way ANOVA with post hoc

for significance. Mean values +/- SEM are plotted. ns = no significance, *p<0.05, **p<0.01, ***p<0.005. n=8-10 animals per group, both males and females used.

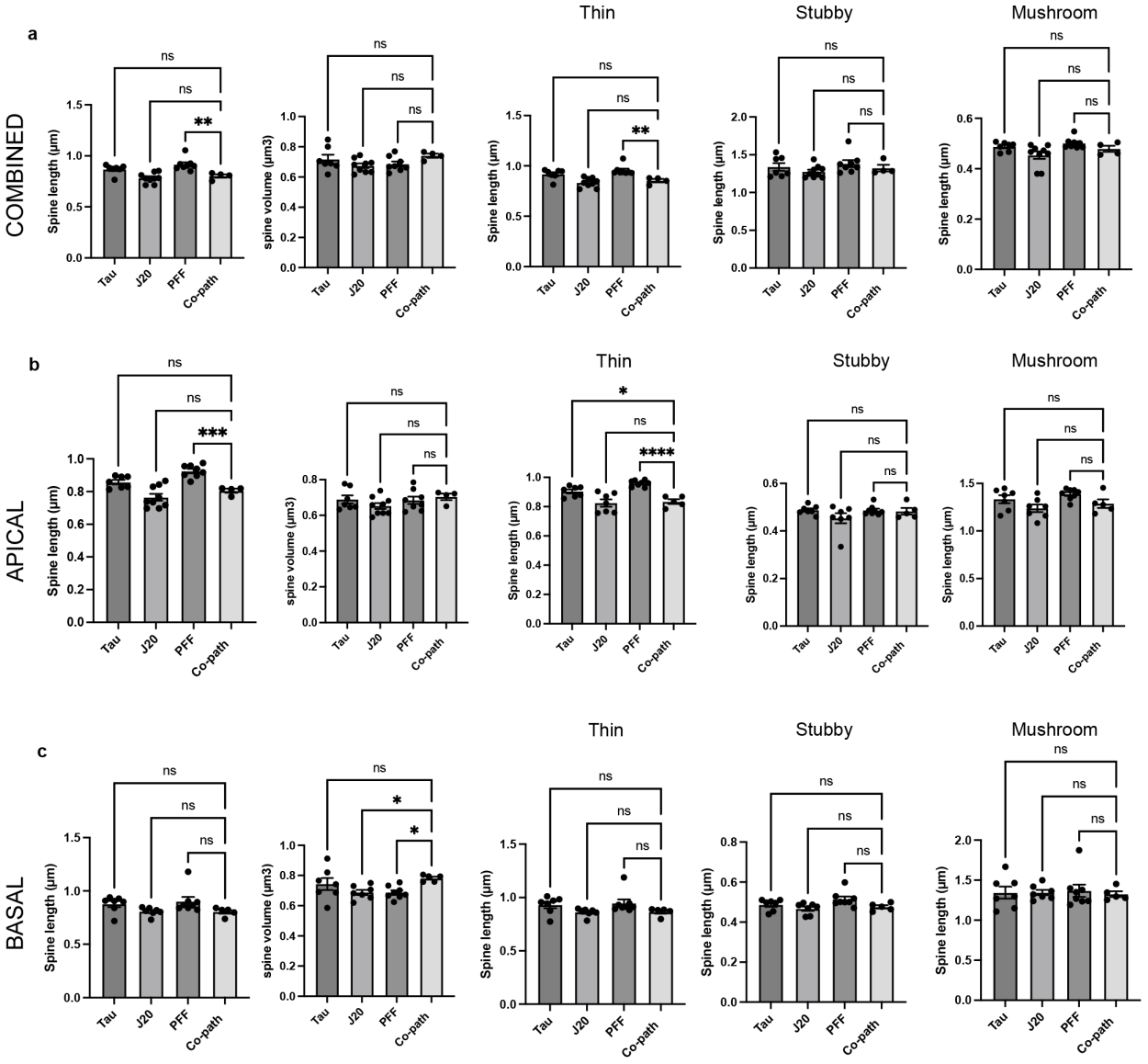

Supplemental Figure 3. Assessment of synapse integrity in the hippocampus of co-pathology and single pathology mice at 6MPI. Dendritic spine morphology was assessed in the CA1 region of hippocampus on pyramidal neurons and measures of total spine length and spine volume for all spines and for thin, stubby and mushroom subgroups are plotted from (a) combined (both apical

1365 and basal), (b) apical only or (c) basal only dendrites. One-way ANOVA with post hoc for
1366 significance. Mean values +/- SEM are plotted. ns = no significance, *$p<0.05$, **$p<0.01$,
1367 ***$p<0.005$. n=8-10 animals per group, both males and females used.
1368

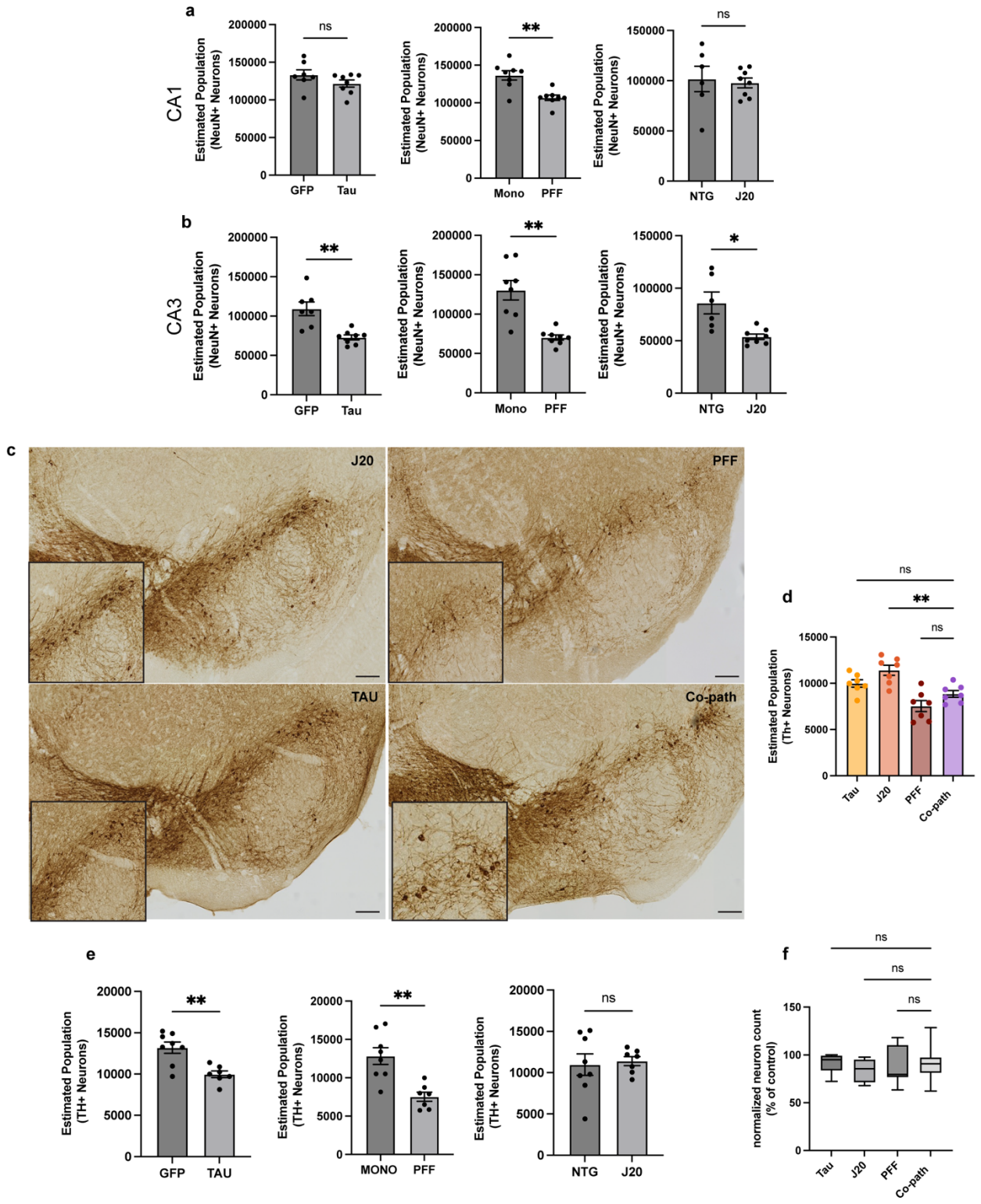

1369

1370 **Supplemental Figure 4. Unbiased stereology for quantification of NeuN+ neurons in the**

1371 **hippocampus (single pathology and controls) and Tyrosine Hydroxylase positive neurons in**

1372 **the substantia nigra pars compacta (SNpc) at 6MPI.** (a,b) Estimated population of NeuN+
1373 neurons of co-pathology and single pathology CA1 or CA3 compared to their individual controls.
1374 (c) TH+ neurons (brown) in the SNpc of single pathology and co-pathology brains. (d) Unbiased
1375 stereology was used to quantify the number of TH+ neurons in the SNpc in the co-pathology mouse
1376 model compared to Tau, J20 and PFF single pathology brains. All images taken at 20X. Scale bars
1377 = 100µm. Student's t-test or One-way ANOVA with post hoc for significance. Mean values +/-
1378 SEM are plotted. Ns = no significance, **$p<0.01$, ***$p<0.005$, ****$p<0.0001$. n=7-8 animals per
1379 group, both males and females used.
1380

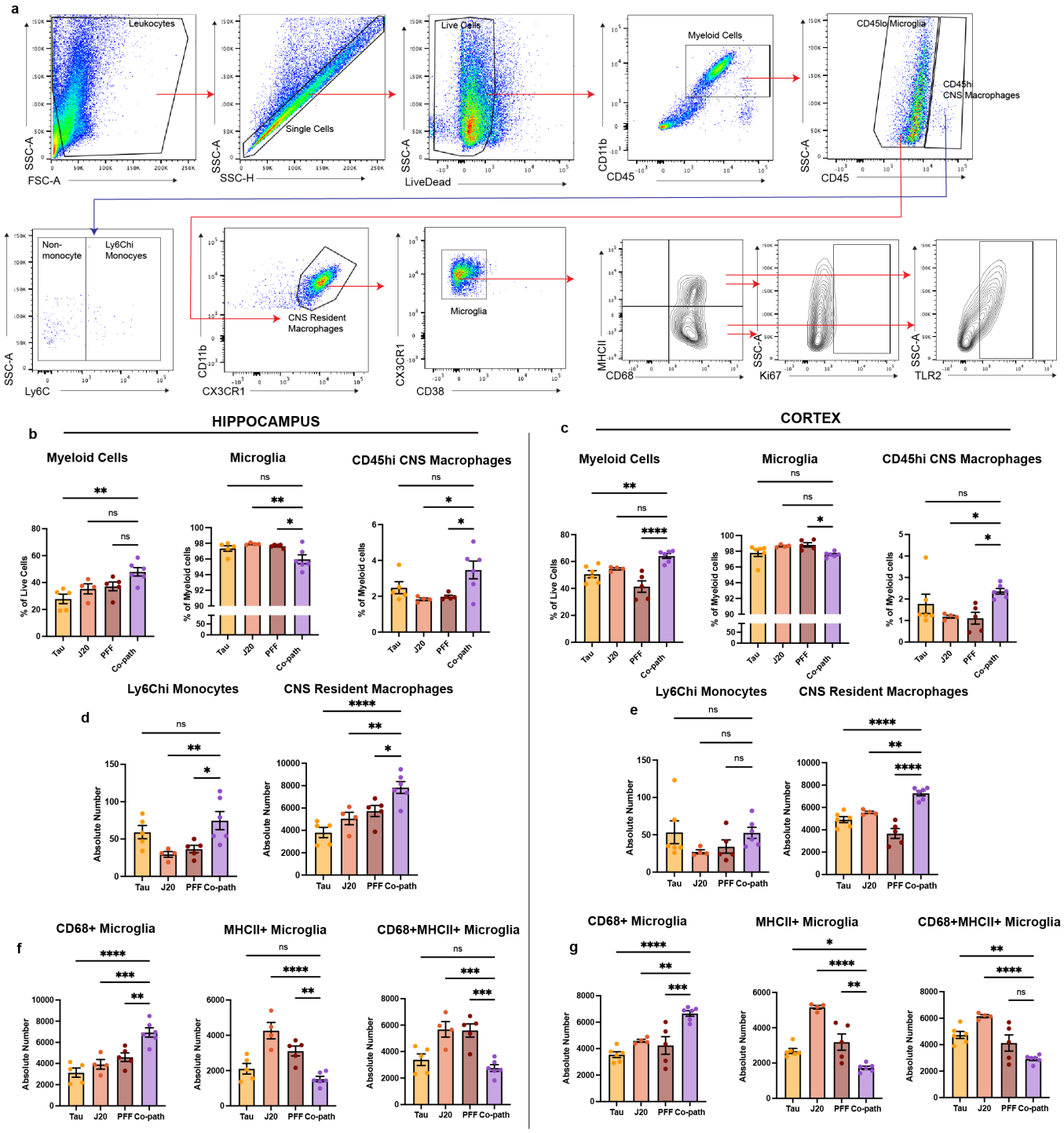

1381

1382 **Supplemental Figure 5. Myeloid cell flow cytometry gating, validation and quantification in**

1383 **co-pathology and single pathology animals.** (a) Gating strategy for flow cytometry analysis of

1384 microglia. (b) Quantification of proportion of myeloid cells, microglia and infiltrating

1385 monocytes/CNS resident macrophages in the co-pathology model hippocampus and (c) cortex
1386 compared to single pathology brains. (d,e) absolute number of CD68+ microglia, MHCII+
1387 microglia and MHCII+CD68+ microglia in the hippocampus and cortex of single pathology and
1388 co-pathology brains. Analyzed using One-way ANOVA. Mean values +/- SEM are plotted.
1389 *$p<0.05$, **$p<0.01$, ***$p<0.005$. n=5-6/group, with two brain regions pooled per sampled, both
1390 males and females included in analysis.
1391

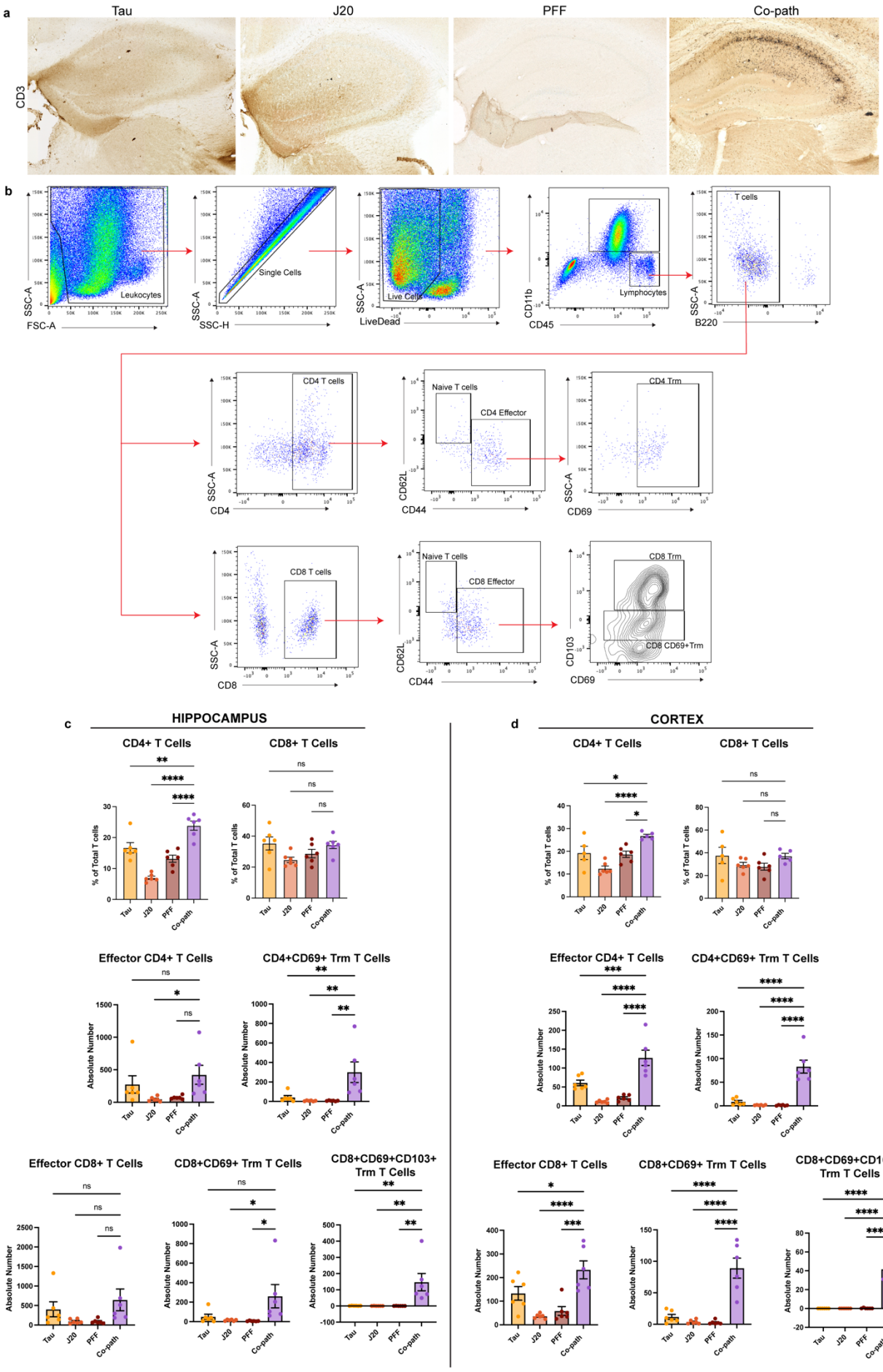
a
Tau
J20
PFF
Co-path
CD3
b
Leukocytes
Single Cells
Live Cells
Lymphocytes
T cells
SSC-A
FSC-A
SSC-H
LiveDead
CD11b
CD45
B220
CD4 T cells
Naive T cells
CD4 Effector
CD4 Trm
CD4
CD44
CD62L
CD69
CD8 T cells
CD8 Effector
CD8 Trm
CD8 CD69+Trm
CD8
CD103
c
HIPPOCAMPUS
CD4+ T Cells
CD8+ T Cells
% of Total T cells
Effector CD4+ T Cells
CD4+CD69+ Trm T Cells
Absolute Number
Effector CD8+ T Cells
CD8+CD69+ Trm T Cells
CD8+CD69+CD103+ Trm T Cells
d
CORTEX
Tau
J20
PFF
Co-path
ns

1393 **Supplemental Figure 6. T cell flow cytometry gating, validation and quantification in co-**
1394 **pathology and single pathology animals.** (a) Representative images showing CD3+ staining
1395 (nickel) from Tau, J20, PFF and co-pathology brains. (b) Gating strategy for flow cytometry
1396 analysis of T cells. (c) Quantification from flow cytometry of proportion of CD4 and CD8 T cells,
1397 and absolute number of effector CD4 and CD8 T cells, and Trm T cells in the hippocampus and
1398 (d) cortex. Analyzed using One-way ANOVA. Mean values +/- SEM are plotted. *$p<0.05$,
1399 **$p<0.01$, ***$p<0.005$. n=5-6/group, with two brain regions pooled per sampled, both males and
1400 females included in analysis.

1401

1402